Publications of the Astronomical Society of the Pacific, 137:044203 (24pp), 2025 April https://doi.org/10.1088/1538-3873/adcaeb

Low-luminosity Type IIP Supernovae from the Zwicky Transient Facility Census of the Local Universe. I. Luminosity Function, Volumetric Rate

Kaustav K. Das[1], Mansi M. Kasliwal[1], Christoffer Fremling[2], Jesper Sollerman[3], Daniel A. Perley[4], Kishalay De[5], Anastasios Tzanidakis[6], Tawny Sit[7], Scott Adams[1], Shreya Anand[8], Tomas Ahumuda[1], Igor Andreoni[9], Seán Brennan[3], Thomas Brink[10], Rachel J. Bruch[11], Ping Chen[11], Matthew R. Chu[10], David O. Cook[12], Sofia Covarrubias[1], Aishwarya Dahiwale[1], Nicholas Earley[1], Anna Y. Q. Ho[13], Avishay Gal-Yam[11], Anjasha Gangopadhyay[3], Erica Hammerstein[14], K-Ryan Hinds[4], Viraj Karambelkar[1], Yihan Kong[15], S. R. Kulkarni[1], Theophile Jegou du Laz[1], Chang Liu[16,17], William Meynardie[1], Adam A. Miller[16,17,18], Guy Nir[10], Kishore C. Patra[10], Priscila J. Pessi[3], R. Michael Rich[19], Nabeel Rehemtulla[16,17,18], Sam Rose[1], Ben Rusholme[12], Steve Schulze[17], Yashvi Sharma[1], Avinash Singh[3], Roger Smith[2], Robert Stein[1], Milan Sharma Mandigo-Stoba[19], Nora L. Strotjohann[11], Yu-Jing Qin[1], Jacob Wise[4], Avery Wold[12], Lin Yan[2], Yi Yang[20], Yuhan Yao[10], and Erez Zimmerman[11]

[1] Cahill Center for Astrophysics, California Institute of Technology, MC 249-17, 1200 E California Boulevard, Pasadena, CA 91125, USA; kdas@astro.caltech.edu
[2] Caltech Optical Observatories, California Institute of Technology, Pasadena, CA 91125, USA
[3] The Oskar Klein Centre, Department of Astronomy, Stockholm University, AlbaNova, SE-10691 Stockholm, Sweden
[4] Astrophysics Research Institute, Liverpool John Moores University, IC 2, Liverpool L3 5RF, UK
[5] MIT-Kavli Institute for Astrophysics and Space Research, 77 Massachusetts Ave., Cambridge, MA 02139, USA
[6] Department of Astronomy and the DiRAC Institute, University of Washington, 3910 15th Avenue NE, Seattle, WA 98195, USA
[7] Department of Astronomy, The Ohio State University, Columbus, OH 43210, USA
[8] Kavli Institute for Particle Astrophysics and Cosmology, Stanford University, Stanford, CA 94305-4085, USA
[9] Department of Physics and Astronomy, University of North Carolina at Chapel Hill, Chapel Hill, NC 27599-3255, USA
[10] Department of Astronomy, University of California, Berkeley, CA 94720-3411, USA
[11] Department of Particle Physics and Astrophysics, Weizmann Institute of Science, 234 Herzl St, 76100 Rehovot, Israel
[12] IPAC, California Institute of Technology, 1200 E. California Blvd, Pasadena, CA 91125, USA
[13] Department of Astronomy, Cornell University, Ithaca, NY 14853, USA
[14] Department of Astronomy, University of Maryland, College Park, MD 20742, USA
[15] Institute for Astronomy, University of Hawaii at Manoa, Honolulu, USA
[16] Department of Physics and Astronomy, Northwestern University, 2145 Sheridan Rd, Evanston, IL 60208, USA
[17] Center for Interdisciplinary Exploration and Research in Astrophysics (CIERA), 1800 Sherman Ave., Evanston, IL 60201, USA
[18] NSF-Simons AI Institute for the Sky (SkAI), 172 E. Chestnut St., Chicago, IL 60611, USA
[19] Department of Physics & Astronomy, University of California Los Angeles, 430 Portola Plaza, Los Angeles, CA 90095-1547, USA
[20] Department of Physics, Tsinghua University, Beijing 100084, People's Republic of China
Received 2025 February 23; revised 2025 April 7; accepted 2025 April 9; published 2025 April 29

Abstract

We present the luminosity function and volumetric rate of a sample of Type IIP supernovae (SNe) from the Zwicky Transient Facility Census of the Local Universe survey (CLU). This is the largest sample of Type IIP SNe from a systematic volume-limited survey to-date. The final sample includes 330 Type IIP SNe and 36 low-luminosity Type II (LLIIP) SNe with $M_{r,\mathrm{peak}} > -16$ mag, which triples the literature sample of LLIIP SNe. The fraction of LLIIP SNe is 19^{+3}_{-4}% of the total CLU Type IIP SNe population (8^{+1}_{-2}% of all core-collapse SNe). This implies that while LLIIP SNe likely represent the fate of core-collapse SNe of 8–12 $M_{\odot}$ progenitors, they alone cannot account for the fate of all massive stars in this mass range. To derive an absolute rate, we estimate the ZTF pipeline efficiency as a function of the apparent magnitude and the local surface brightness. We derive a volumetric rate of $(3.9^{+0.4}_{-0.4}) \times 10^4$ Gpc^{-3} yr^{-1} for Type IIP SNe and $(7.3^{+0.6}_{-0.6}) \times 10^3$ Gpc^{-3} yr^{-1} for LLIIP SNe. Now that the rate of LLIIP SNe is robustly derived, the unresolved discrepancy between core-collapse SN rates and star formation rates cannot be explained by LLIIP SNe alone.

Unified Astronomy Thesaurus concepts: Supernovae (1668); Core-collapse supernovae (304); Type II supernovae (1731); Surveys (1671); Transient sources (1851); Massive stars (732)

1. Introduction

Core-collapse supernovae (CCSNe), the explosive endpoints of massive stars, drive chemical evolution in galaxies, provide impetus for the formation of new generations of stars, and leave behind neutron star or black hole remnants. Despite the discovery of over 10,000 SNe, the fate of stars at the low-mass end of CCSNe, with progenitor initial masses of $\approx$8–12 $M_{\odot}$, is not well understood (e.g., see Janka 2012; Sukhbold et al. 2016). Exploring this mass range is important, because it probes the boundary between whether a star has a large enough mass to form a neutron star from its central core or, instead, leaves behind a white dwarf. Also, it is uncertain whether stars in this mass range undergo iron core-collapse from Red Supergiants (RSG) or if electron capture in super-Asymptotic Giant Branch (sAGB) stars drives the SN explosions (Nomoto 1984; Jerkstrand et al. 2018; Leung & Fuller 2020; Kozyreva et al. 2021).

Stars in the 8–12 $M_{\odot}$ range exhibit a distinctly different core structure compared to those with higher progenitor mass, characterized by significantly lower compactness (Sukhbold et al. 2016). The evolution of such stars is more complex to model than at $>12\,M_{\odot}$ due to the development of thermal pulses that are numerically challenging to follow, and highly uncertain late-time mass-loss (e.g., Miyaji et al. 1980; Woosley & Heger 2015). The lowest mass CCSNe have steep density gradients outside their degenerate cores, liberate less gravitational binding energy, have lower neutrino luminosities, and ultimately are associated with lower luminosities, explosion energy and nickel yield (Janka 2012; Müller 2016; Burrows et al. 2019, 2024; Eldridge et al. 2019; Stockinger et al. 2020; Burrows & Vartanyan 2021; Sandoval et al. 2021; Barker et al. 2022).

It is critical to understand this faint end of the core-collapse luminosity function, constrain their rates and couple the stellar evolution initial mass function (IMF) to the known SN populations. Determining the SN rate and tying it to the mass boundary between stars that do and do not explode as SNe is vital for determining the number of neutron stars, galactic chemical evolution and dust evolution models, and the total energy released by SNe into the environment. The CCSN distribution traces the formation of massive stars and the CCSN rate should match the massive star formation rate using the known star formation rate density and IMF, given our current understanding of stellar evolution. However, there is an apparent discrepancy between the two absolute rates with the star formation implying a much higher CCSN rate than is observed. This ongoing debate has been discussed extensively in the literature (e.g., Horiuchi et al. 2011, 2013; Botticella et al. 2012; Cappellaro et al. 2015; Xiao & Eldridge 2015; Jencson et al. 2019b). One possibility is that this disagreement arises from a missing population of low-luminosity CCSNe.

One such class of faint CCSNe is low-luminosity Type IIP SNe (LLIIP SNe), which likely represent the explosions of 8–12 $M_{\odot}$ progenitor stars. LLIIP SNe exhibit a faint peak luminosity, defined here as $M_{r,\mathrm{peak}} \geqslant -16$ mag, motivated by prior literature (e.g., Spiro et al. 2014). Recent studies, based on pre-explosion images of SNe 2005cs, 2008bk, 2018aoq, 2022acko (Maund et al. 2005; Li et al. 2006; Mattila et al. 2008; O'Neill et al. 2019; Van Dyk et al. 2023) also show that SNe with r-band peak >-16 mag have progenitor mass estimates less than 11 $M_{\odot}$, while those with brighter peak have progenitor masses $>12\,M_{\odot}$(see Figure 12 in Appendix A). The nickel mass ($\sim$0.005 $M_{\odot}$) of LLIIP SNe is an order of magnitude lower than that typically found in standard Type II SNe (e.g., Rodríguez et al. 2021). Additionally, LLIIP SNe are characterized by slow expansion velocities (approximately 1300–2500 km s^{-1} at 50 days after the explosion), indicating low explosion energies. The low energy and low nickel mass could be explained by the explosion of 8–12 $M_{\odot}$ progenitors. This is also favored by lightcurve simulations (Fraser et al. 2011; Pumo et al. 2017), evolutionary numerical simulations of low mass RSGs (Lisakov et al. 2017), and nebular spectroscopy (Jerkstrand et al. 2018). A correlation is also observed between the explosion energy, nickel mass and progenitor mass estimates from pre-SN imaging (Eldridge et al. 2019), where lower-mass progenitors ($<12\,M_{\odot}$) are associated with lower nickel mass ($<0.01\,M_{\odot}$) and lower explosion energy ($<2 \times 10^{50}$ erg s^{-1}).

However, there are only about a dozen such objects presented in the literature (Turatto et al. 1998; Spiro et al. 2014; Jäger Zoltán et al. 2020; Müller-Bravo et al. 2020; Reguitti et al. 2021; Yang et al. 2021; Kozyreva et al. 2022; Valerin et al. 2022; Bostroem et al. 2023; Teja et al. 2024; Dastidar et al. 2025). For a Salpeter IMF (Salpeter 1955), around 50% of the potential CCSN progenitors reside in the 8–12 $M_{\odot}$ mass range. Given this fact, it is surprising that such SNe are rarely detected. What do half of the stars that undergo core-collapse explode as? It is likely that this deficit of discovery can be explained by the connection between these relatively low-mass progenitors and the occurrence of low-luminosity SNe, which are more difficult to detect and classify.

In this series of three papers, we present the analysis of a sample of 36 LLIIP SNe detected by Zwicky Transient Facility (ZTF) as part of the Census of the Local Universe (CLU) Survey, which roughly triples the number of existing LLIIP SNe in the literature. The focus of the first paper is to estimate their luminosity function and volumetric rates.

To place these results in a broader context, we also present a sample of 330 Type IIP SNe, obtained from the largest systematic volume-limited SN survey to date. The previous Type II SNe sample from a volume-limited sample survey includes 62 Type II SNe from the Lick Observatory Supernova Search (LOSS; Li et al. 2011). Other Type II samples from systematics surveys include 50 Type II SNe from the

Panoramic Survey Telescope and Rapid Response System (PS1; Sanders et al. 2015), 34 Type IIP SNe from the Sloan Digital Sky Survey II Supernova Survey (SDSS-II SNS; Taylor et al. 2014) and 21 Type II SNe from the Caltech Core-collapse SN Project (CCCP; Arcavi et al. 2012).

In Section 2.2, we define the sample selection criteria. The data obtained and the extinction correction method are described in Sections 3 and 4, respectively. In Sections 5 and 6, we estimate the luminosity function and the volumetric rate of LLIIP SNe and compare with the overall CLU Type IIP SN population. We discuss the implications of the measured LLIIP rates in Section 7 and conclude in Section 8. In companion Papers II and III, we will present the analysis of their lightcurves and nebular spectra, respectively.

2. Sample Selection

2.1. Census of the Local Universe

ZTF conducts an optical time-domain survey with the 48 inch Schmidt telescope (P48) situated at Palomar Observatory (Bellm et al. 2019; Graham et al. 2019; Dekany et al. 2020). The ZTF CLU experiment aims to build a comprehensive spectroscopic sample of transients in the local Universe. To accomplish this, we match the hosts of these transients with the galaxy catalog from the Census of the Local Universe (Cook et al. 2019). This catalog contains around 234,500 galaxies with established distances, compiled from pre-existing spectroscopic galaxy surveys and the CLU-Hα survey (refer to Cook et al. 2019 for further details).

The CLU experiment is designed as a volume-limited SN survey where sources at less than 150 Mpc ($z \leqslant 0.033$) and spatially coincident with (within 30 kpc) or visibly associated with a galaxy in the CLU catalog were assigned for spectroscopic follow-up for classification. For more detailed discussion of the CLU experiment filtering, see De et al. (2020). The filter is implemented on the Global Relay of Observatories Watching Transients Happen (`GROWTH`) Marshal (Kasliwal et al. 2019) and the `Fritz` Marshal (van der Walt et al. 2019; Coughlin et al. 2023), both of which are web portals designed for vetting and coordinating transient follow-up observations.

After passing through the CLU filter, the transients are allocated for spectroscopic classification using: the Spectral Energy Distribution Machine (SEDM; Blagorodnova et al. 2018; Kim et al. 2022) at the Palomar 60 inch telescope, the Double-Beam Spectrograph (DBSP; Oke & Gunn 1982) at the Palomar 200 inch Hale telescope, and the Low-Resolution Imaging Spectrometer (LRIS; Oke et al. 1995). In this paper, we consider SNe saved to the CLU experiment starting from 2018 October 1 until 2024 April 1. We exclude the targets saved to ZTF in 2020 as the CLU experiment was inactive during that year. A total of 1745 SNe saved to CLU were classified during this interval.

2.2. Sample of LLIIP SNe

We apply the following selection criteria on the ZTF SN sample obtained from the CLU survey:

1. *Type II Classification*. From the CLU sample, 727 candidates classified as Type II (including subtypes IIP, II, IIL, II-norm, and II-pec) were selected.
2. *Peak Magnitude*. A Gaussian process fit was applied to the forced photometry light curves, and the sample was restricted to those with a peak magnitude $m_{\mathrm{peak}_r} < 20$ mag, resulting in 719 candidates. The peak magnitude and other lightcurve parameters are measured on this GP fit (see Section 3.1 for details.). The 20 mag cut is chosen as the pipeline recovery efficiency and classification completeness drops below 80% for alerts fainter than 20 mag (see Section 5).
3. In order to constrain the *r*-band peak, we first require that the candidates have more than 10 detections, reducing the sample to 626. We also require that the candidates pass any one of the following conditions:
   (a) Candidates with at least one detection before the peak and one after the peak, and for which the duration between the last non-detection and the first detection ($t_{\mathrm{firstdet}} - t_{\mathrm{lastnon-det}}$) was $\leqslant$20 days.
   (b) If $t_{\mathrm{firstdet}} - t_{\mathrm{lastnon-det}} \geqslant 20$ days, then candidates with more than 10 pre-peak detections and more than 2 post-peak detections, as well as a magnitude difference $\mathrm{mag}_{\mathrm{firstdet}} - \mathrm{mag}_{\mathrm{peak}} > 1$ mag, were considered.
   (c) For candidates where the first detection corresponds to the peak, the last non-detection had to occur within 10 days of the first detection.

394 candidates pass this quality cut.

4. *Plateau Criterion*. Candidates were required to show a plateau phase, defined as a duration of $\geqslant$40 days with a drop of less than 1 mag, resulting in a sample of 330 candidates.
5. *Peak Absolute Magnitude*. To obtain the absolute magnitudes, we use the distance modulus calculated from the host redshift assuming a cosmological model with $\Omega_M = 0.3$, $\Omega_\Lambda = 0.7$, and $h = 0.7$. For galaxies closer than 25 Mpc, we correct for the Virgo, Great Attractor, and Shapley supercluster infall based on the NASA Extragalactic Database object page (NED[21]; G. Helou et al. 1991). We ignore corrections due to peculiar motions for galaxies farther than 25 Mpc. If the peculiar motion of the galaxy is $\sim$300 km s^{-1}, then the error of the peak magnitude is $\leqslant$0.1 mag. Table B1 lists the distances used for the nearby galaxies and their references. We apply a K-correction of $2.5 \times \log(1+z)$ for all the SNe in our sample. The LLIIP sample is

[21] https://ned.ipac.caltech.edu/

Table 1
Summary Table of the Sample Selection Criteria

Step	Criteria	# Candidates
1	SNe in CLU classified as Type II (IIP, II, II-norm, II-pec)	727
2	Gaussian process fit to forced photometry lightcurves, $m_{\mathrm{peak}_r} < 20$ mag	719
3	Number of detections $(N_{\mathrm{pre-peak}} + N_{\mathrm{post-peak}}) > 10$	
3A	If first detection is the peak, require that the last non-detection is within 10 days of first detection	
3B	$\geqslant$1 detection before peak and $\geqslant$1 detection after peak and $t_{\mathrm{firstdet}} - t_{\mathrm{lastnon-det}} \leqslant 20$ days	394
3C	If $t_{\mathrm{firstdet}} - t_{\mathrm{lastnon-det}} \geqslant 20$ days, $N_{\mathrm{pre-peak}} > 10$, $N_{\mathrm{post-peak}} > 2$, $\mathrm{mag}_{\mathrm{firstdet}} - \mathrm{mag}_{\mathrm{peak}} > 1$ mag	
4	Criteria for plateau: There should be a duration of 40 days with a drop of <1 mag	330
5	LLIIP: Peak absolute magnitude $\geqslant -16$ mag (no host extinction)	48
	LLIIP: Peak absolute magnitude $\geqslant -16$ mag (after host extinction)	36

restricted to those with a peak absolute magnitude less luminous than −16 mag, leaving 48 LLIIP SN candidates.

6. *Host Extinction Correction*. Finally, after correcting for host galaxy extinction (see Section 4 for details), 36 LLIIP SNe remained in the final sample.

The summary of the selection criteria and the sample are provided in Tables 1 and 2 respectively. The distribution of the number of SNe as a function of peak absolute magnitude is shown in Figure 1. A complementary ZTF experiment is the magnitude-limited Bright Transient Survey (BTS; Fremling et al. 2020; Perley et al. 2022), aimed at classifying transients brighter than a peak apparent magnitude of 18.5 mag without any redshift cut. 62 SNe in our sample are also part of the Type II SN sample of the BTS survey (Y. Qin et al. 2025, in preparation; K. Hinds et al. 2025, in preparation).

3. Data

In this section, we describe the photometric and spectroscopic data used.

3.1. Optical Photometry

We perform forced point-spread function photometry on the ZTF difference images at the location of these SNe using the ZTF forced-photometry service developed by Masci et al. (2019, 2023) in g and r bands. For this work, we consider anything less than a 3σ detection an upper limit. We used a Gaussian Process (GP) algorithm[22] (Ambikasaran et al. 2015) to interpolate the photometric measurements and measure the slope. Figure 2 shows the lightcurves of SNe 2023wcr and 2024wcs as examples. The vertical dashed red line shows the epoch of first detection, and the vertical dashed gray line shows the epoch of last non-detection. The explosion epoch is defined to be midway between the epoch of first detection and last non-detection. The epochs of peak r- and g-band magnitudes are shown by the vertical solid red and blue lines. The photometry data, lightcurve plots, and spectroscopy of all SNe in the sample will be made available on WISEREP and Zenodo after publication.

3.2. Optical Spectroscopy

For each transient, at least one spectrum is usually obtained close to the peak luminosity to establish a spectroscopic classification as described in Section 2.1. We employ the `SuperNova Identification` (`SNID`; Blondin & Tonry 2007) code for these classifications. For spectra that show host galaxy contamination, we utilize `superfit` (Howell et al. 2005). The reduction of DBSP spectra follows the procedures outlined in Bellm & Sesar (2016) and Roberson et al. (2022), while the SEDM data reductions are detailed in Rigault et al. (2019). The LRIS spectra were reduced using the automated LPIPE (Perley 2019) pipeline.

We also make use of spectra from the Alhambra Faint Object Spectrograph and Camera at the Nordic Optical Telescope (NOT; Djupvik & Andersen 2010) and from the Spectrograph for the Rapid Acquisition of Transients (SPRAT; Piascik et al. 2014) on the Liverpool Telescope. The NOT data reduction utilized the PyNOT[23] and PypeIt (Prochaska et al. 2020) pipelines. The SPRAT data is processed using a pipeline based on FrodoSpec (Barnsley et al. 2012).

4. Extinction Correction

Extinction is divided into two components. The first component represents dust extinction from the Milky Way, while the second component accounts for extinction originating from the host galaxies of the SNe. To correct for Galactic extinction, we employ the reddening maps provided by Schlafly & Finkbeiner (2011), the extinction law described by Cardelli et al. (1989) and a value of $R_V = 3.1$.

[22] https://george.readthedocs.io/

[23] https://github.com/jkrogager/PyNOT

Table 2
Summary Table of the CLU Type II SN Sample

Name	R.A. (hh:mm:ss)	Decl. (dd:mm:ss)	Redshift	t_{exp} (MJD)	1st Detection (MJD)	Peak mag$_r$ (mag)	$A_{V,MW}$ (mag)	$A_{V,host}$ (mag)
ZTF18abnxfve/AT2018lrz	22:29:52.72	+36:43:50.1	0.025	58347.8	58349.3	−15.94	0.30	0.00
ZTF18abrzbtb/SN 2018ggu	07:43:04.67	+50:17:22.2	0.019	59120.0	59120.5	−15.66	0.19	0.00
ZTF19aaabzpt/SN 2018lab	06:16:26.51	−21:22:32.4	0.009	58479.3	58487.3	−15.81	0.24	0.71
ZTF19aalycsv/AT2019txj	10:48:39.19	+76:48:05.3	0.023	58543.3	58546.2	−15.27	0.07	0.00
ZTF19aamwhat/SN 2019bzd	14:47:32.03	−19:45:57.7	0.008	58559.7	58568.4	−15.83	0.24	0.07
ZTF19aatmadu/AT2019esn	14:51:56.11	+51:15:51.2	0.027	58602.4	58605.4	−16.00	0.06	0.00
ZTF19abalqkq/AT2019khq	17:50:41.76	+14:49:26.3	0.014	58645.9	58650.3	−15.76	0.26	1.63
ZTF19abctzkc/AT2019tti	00:18:59.83	+08:46:28.2	0.019	58644.4	58646.4	−15.67	0.55	0.21
ZTF19abejaiy/SN 2019krp	14:07:33.70	+14:38:03.3	0.017	58670.2	58671.2	−15.45	0.04	0.00
ZTF19ablfoqa/AT2019tya	02:09:38.03	+01:33:06.7	0.032	58694.0	58694.5	−15.93	0.08	0.00
ZTF19abllxfy/AT2019ttl	21:52:43.47	+38:56:00.8	0.020	58682.9	58690.3	−15.36	0.88	0.00
ZTF19acalxgp/AT2019qiq	23:44:56.09	−04:16:33.1	0.029	58735.4	58737.3	−15.86	0.12	0.00
ZTF21aabfwwl/SN 2021iy	11:18:31.68	−06:16:40.5	0.014	59217.9	59219.4	−15.55	0.14	0.00
ZTF21aaobkmg/SN 2021eui	19:20:55.80	+43:07:14.6	0.015	59273.5	59276.5	−15.34	0.28	0.00
ZTF21aaqgmjt/SN 2021gmj	10:38:47.27	+53:30:30.3	0.003	59292.3	59293.2	−15.02	0.06	0.00
ZTF21abbomrf/AT2020ghq	14:45:20.59	+38:44:18.5	0.015	59347.8	59349.2	−15.72	0.03	0.00
ZTF21abglcxm/SN 2021qcs	15:29:22.82	−12:14:54.4	0.011	59377.3	59378.2	−15.65	0.43	0.42
ZTF21acdoyqt/SN 2021zgm	18:35:48.34	+22:27:45.2	0.013	59479.2	59480.1	−15.51	0.44	0.00
ZTF22aaahubo/AT2022cru	08:23:26.30	−04:55:06.5	0.023	59575.4	59600.3	−15.89	0.12	0.00
ZTF22aakdbia/SN 2022jzc	12:05:28.66	+50:31:36.8	0.002	59714.3	59715.2	−14.91	0.05	0.57
ZTF22aanrqje/SN 2022mji	09:42:54.06	+31:51:03.6	0.004	59732.7	59741.2	−15.00	0.05	0.85
ZTF22aaywnyg/SN 2022pru	11:59:07.65	+52:41:58.5	0.004	59787.7	59797.2	−15.42	0.07	0.00
ZTF22aazmrpx/SN 2022raj	02:03:17.52	+29:14:04.9	0.012	59798.4	59800.4	−15.20	0.15	0.00
ZTF22abssiet/SN 2022zmb	10:38:43.18	+56:33:14.4	0.014	59885.5	59887.5	−15.72	0.02	0.07
ZTF22abvaetz/SN;2022aang	07:59:21.83	+18:06:40.9	0.016	59894.5	59901.5	−15.44	0.08	0.00
ZTF22abyivoq/SN 2022acko	03:19:38.98	−19:23:42.8	0.006	59917.8	59922.2	−15.83	0.08	0.00
ZTF23aaarmtb/SN 2023qh	09:07:15.44	+37:12:54.8	0.024	59947.4	59957.4	−15.89	0.06	0.00
ZTF23aackjhs/SN 1995al	09:50:56.03	+33:33:11.0	0.005	59989.8	59992.3	−14.88	0.04	0.07
ZTF23aagkajy/AT2023gdt	10:30:10.64	+43:21:23.4	0.014	60050.2	60051.2	−15.42	0.03	0.71
ZTF23aajrmfh/SN 2023ijd	12:36:32.47	+11:13:19.7	0.007	60078.2	60079.0	−15.39	0.09	0.00
ZTF23aamzlzc/AT2023kne	17:25:19.11	+58:49:02.6	0.028	60095.4	60097.3	−15.81	0.10	0.00
ZTF23aaqwpio/AT2023nca	16:39:26.36	+11:12:45.3	0.023	60129.3	60135.2	−15.61	0.14	0.00
ZTF23aasyvbf/SN 2023nmh	00:37:38.73	−04:16:53.2	0.020	60142.4	60144.5	−15.93	0.10	0.00
ZTF23abnogui/SN 2023wcr	12:23:31.29	+74:57:01.3	0.005	60240.5	60244.5	−15.58	0.09	0.00
ZTF23abvommm/SN 2023acbr	02:27:03.18	−09:25:02.3	0.016	60300.7	60305.2	−15.57	0.08	0.00
ZTF24aabppgn/SN 2024wp	11:24:39.25	+14:56:52.9	0.014	60320.5	60325.5	−15.52	0.10	0.00
ZTF24aahwfsa/AT2024fas	10:51:55.36	+37:35:23.9	0.026	60393.4	60396.4	−15.80	0.04	0.00
ZTF24aaplfjd/SN 2024jxm	0:58:01.36	+30:42:23.84	0.016	60460.0	60460.5	−16.00	0.18	0.00

Note. Only the first 45 rows are shown here. The full table is shown in the Appendix D. The peak absolute magnitudes have been measured by assuming Milky Way extinction ($A_{V,MW}$) and host galaxy extinction ($A_{V,host}$) as described in Section 4. The t_{expl} column shows the explosion epoch. The Peak mag$_r$ shows the peak r-band absolute magnitude. A machine-readable version of the full sample table is available in DOI:10.5281/zenodo.14538857.

To estimate the host-galaxy extinction, we use the average $g-r$ color curve of the sample. First, we measure the Na I D absorption lines of the host environment (Poznanski et al. 2012; Stritzinger et al. 2018) when a high SNR SN spectrum is available. To measure the template $g-r$ color, we discard objects with Na I D EW >1 Å. The 1σ scatter is 0.35 mag. The average color and standard deviation (1σ range) are shown by the black solid line and blue shaded region, respectively, in Figure 3. This template is available in DOI:10.5281/zenodo.14538857. We then measure the $A_{V,host}$ assuming that the SN color exceeding the 1σ $g-r$ template is caused by host extinction. 80 out of the 330 Type IIP SNe has $A_{V,host} > 0$. The sample color curve after this correction is shown in the right panel of Figure 3. The remaining 1σ scatter in the $g-r$ color is likely due to intrinsic properties of the SNe, which could be dominated by photospheric temperature differences (e.g., see de Jaeger et al. 2018). Table 2 lists the measured $A_{V,host}$ values.

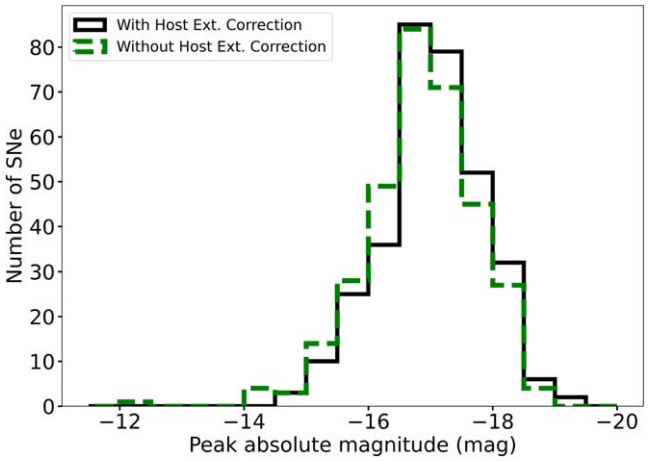

Figure 1. The distribution of the number of SNe in the final ZTF CLU Type IIP sample, consisting of 330 SNe, as a function of peak r-band absolute magnitude, with and without host-extinction correction.

5. Luminosity Function

With the use of our systematic and controlled ZTF CLU event sample, we determine a luminosity function for Type IIP and LLIIP SNe. The CLU LLIIP sample nearly triples the current number of published LLIIP SNe in the literature. Our final sample comprises 330 Type IIP SNe, with 36 (≈11%) LLIIP SNe ($M_r > -16$ mag).

We use the r-band photometry to measure the SN II luminosity function and volumetric rate. A volume correction is applied to the luminosity function by weighting each object by $V_{\rm max} = 1/D^3_{\rm max}$, where $D_{\rm max}$ ($\propto 10^{\frac{1}{5}(20-M_r,{\rm peak})}$) is the farthest distance at which a transient can be detected given a limiting magnitude of 20 mag. For sources detectable past 150 Mpc, $D_{\rm max}$ was set to the maximum CLU experiment distance of 150 Mpc.

We also correct for the CLU spectroscopic completeness and the ZTF pipeline recovery efficiency factor as they are dependent on the apparent magnitude. Of the total of 2064 transients that are saved in CLU, 1745 (84.6%) transients are classified. The overall completeness of the CLU survey as a function of peak apparent magnitude is indicated by the dashed black line in Figure 4. There are 79 transients for which we are uncertain whether they are real transients on the basis of their spectroscopic and photometric properties. If we exclude these, the overall completeness is ∼87% (solid black line). Also, we note that the long-lived nature and relative ease of identifying the Hα P-Cygni feature make Type IIP events easier to classify. So the Type IIP SNe completeness is likely to be higher than the solid black line. As a conservative estimate, for the rest of the paper, we use the spectroscopic completeness depicted by the dashed black line.

The ZTF image subtraction pipeline has two potential sources of inefficiency relevant to this calculation. In each science image, the pipeline actively masks pixels affected by quality criteria, such as saturation from high brightness, cosmic rays, and defective pixels. This dynamic masking does not have a significant effect as Type IIP SNe have long durations (∼100 days) and are eventually detected by the pipeline. A significant issue relates to the decreased efficiency of the image subtraction algorithm for faint alerts and on bright galaxy backgrounds. Here, we model the efficiency of the ZTF pipeline as a function of the alert flux and the ratio of background surface brightness to target flux. To estimate this, we check whether alert photometry exists for a given epoch for which there is a $\geqslant 5\sigma$ forced photometry detection. The local host surface brightness is extracted using PS1 r-band images with a $3''$ radius aperture. To estimate the conditional probability of the ZTF pipeline efficiency, we consider the binary data, X, which represents whether the ZTF pipeline successfully recovers a transient in alerts ($X = 1$) or not ($X = 0$). We model X using the Bernoulli distribution:

$$X \sim \text{Bern}(p),$$

where p is parameterized by a logistic function dependent on the ratio (r) of the host surface brightness and the target flux:

$$p(r) = \frac{1}{1 + \exp(a(r - c))},$$

with a and c representing the model parameters that need to be determined. The logistic function was chosen because it smoothly transitions from 1 to 0 and captures the pipeline efficiency behavior as a function of r. We then estimate the model parameters using the `emcee` package (Foreman-Mackey et al. 2013). The best-fit values of a and c are $a = 1.12^{+0.02}_{-0.02}$ and $c = 0.21^{+0.03}_{-0.03}$ respectively. As expected, the recovery efficiency decreases as this ratio increases. The best-fit efficiency is ∼50% when the host surface brightness and target fluxes are comparable.

We also measure the inefficiency as a function of the apparent magnitude alone, using

$$p(m) = \frac{1}{1 + \exp(b(m - d))},$$

where m is the alert apparent magnitude. The best-fit values obtained are $b = 2.28^{+0.03}_{-0.04}$ mag^{-1} and $d = 20.57^{+0.01}_{-0.01}$ mag. The best fits, and corner plots of the MCMC fit are shown in Figure 5 and Appendix C, respectively. The best-fit efficiency decreases with an increase in target alert apparent magnitude and is ≈80% when the alert magnitude is 20 mag.

We then weight each SN by the corresponding classification completeness factor and the pipeline efficiency factor. The luminosity function thus obtained is shown in Figure 6 in blue. The luminosity function without volume correction is shown by the green dashed lines in Figure 6. After volume-, incompleteness- and pipeline-efficiency correction, the fraction of LLIIP SNe is 19^{+3}_{-4}% of the entire Type II SN population (see

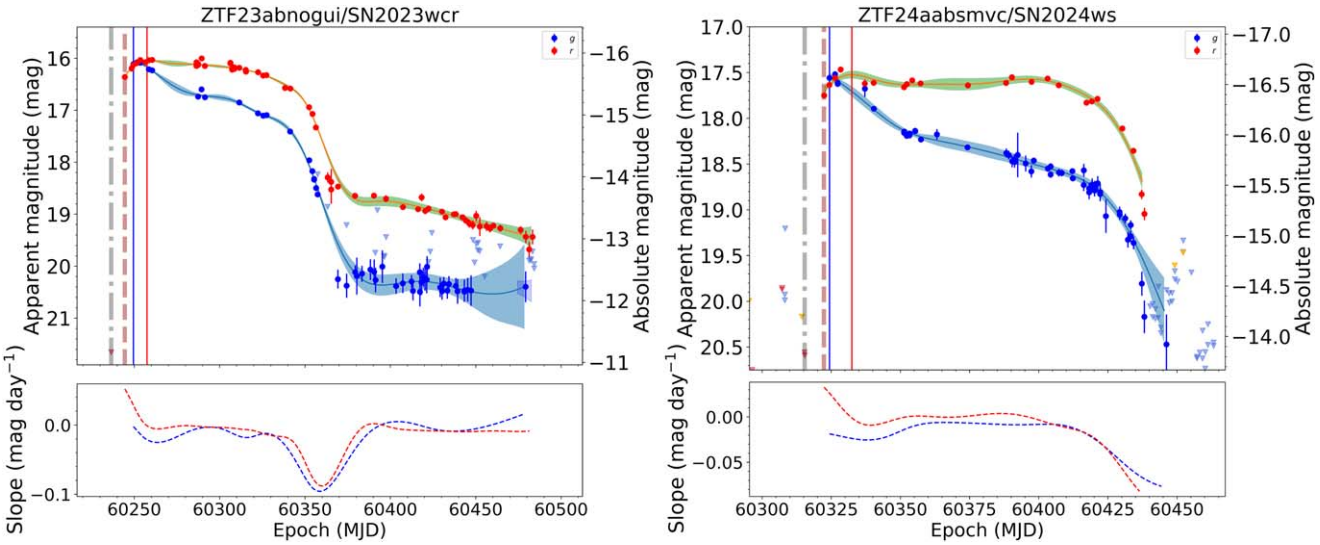

Figure 2. Example of SN light curves and the GP interpolations. The apparent magnitudes have been corrected for Galactic and host extinction. The lower panels show the slope of the light curves, i.e., the derivative of the GP fits, in units of mag per day. The vertical dashed red line shows the epoch of the first detection. The vertical dashed gray line shows the epoch of last non-detection. The vertical solid red and blue lines show the epochs of peak *r*- and *g*-band magnitudes, respectively.

Figure 7). The fraction of Type IIP SNe fainter than −15 mag and −14.5 are <5% and <1.5% respectively.

6. The Volumetric Rate of Type IIP SNe Using Skysurvey

First, we create a template *r*-band lightcurve by compiling the photometry data for all the Type IIP SNe in the sample and apply Gaussian Regression processing (Figure 8). We use the `skysurvey` code[24] to estimate the volumetric rate. `skysurvey` simulates light curves as they would be observed based on a light curve template (using `sncosmo`) and survey plan. The survey plan is constructed using the actual pointing schedule of ZTF, detailing observation times, the filters used, and the sky brightness. Additionally, the simulation incorporates data on CCD outlines to account for data losses caused by chip gaps.

For the selection of simulated SNe II from `skysurvey`, we use the forced photometry-based selection criteria outlined in Section 2.2. We require at least two 5σ detections exceeding 20 mag in brightness. These criteria guarantee detection by the ZTF alert system, allowing the transient to pass the CLU filter, with a distance <150 Mpc to ensure appropriate CLU filter saving and spectroscopic follow-up. Additionally, the lightcurve quality cuts described in Section 2.2 are employed to consistently filter the `skysurvey` sample.

We generate ZTF lightcurves of Type IIP SNe for a range of input volumetric rates (0.1–10.0 $\times$ 10^4 Gpc^{-3} yr^{-1}) for the `skysurvey` simulation up to a distance of 150 Mpc, according to the luminosity function in Figure 6. At each rate, 30 survey plan simulations were conducted. For these simulations, we documented the number of transients that successfully passed the filtering process. The detection estimate for each rate was made by computing the mean number of transients detected from the simulations, with the standard deviation serving as the error estimate. Figure 9 shows the expected number of detected transients along with the fraction of simulations that yield our observed sample size within an error margin of 10% for a given input volumetric rate.

The fraction of simulations matching our sample size follows a skewed Gaussian distribution, which was used to estimate the rate and its uncertainty based on a 68% confidence interval. This analysis yields a volumetric rate of $(2.6^{+0.3}_{-0.3}) \times 10^4$ Gpc^{-3} yr^{-1}.

This raw `skysurvey` rate already accounts for survey conditions such as weather and cadence as we used the real observing history of ZTF to simulate the light curves as they would have been observed. We now apply corrections for spectroscopic incompleteness, pipeline recovery efficiency and galaxy catalog incompleteness. As shown in Section 5, the CLU experiment achieved an overall completeness rate of ≈84%.

In the CLU experiment, our methodology restricts the identification of SNe to those in galaxies where a spectroscopic redshift has been established. Therefore, we must correct the `skysurvey` rate of LLIIP events for galaxy catalog incompleteness. To correct for the incompleteness of the galaxy catalog, we used the redshift completeness factor

[24] https://github.com/MickaelRigault/skysurvey

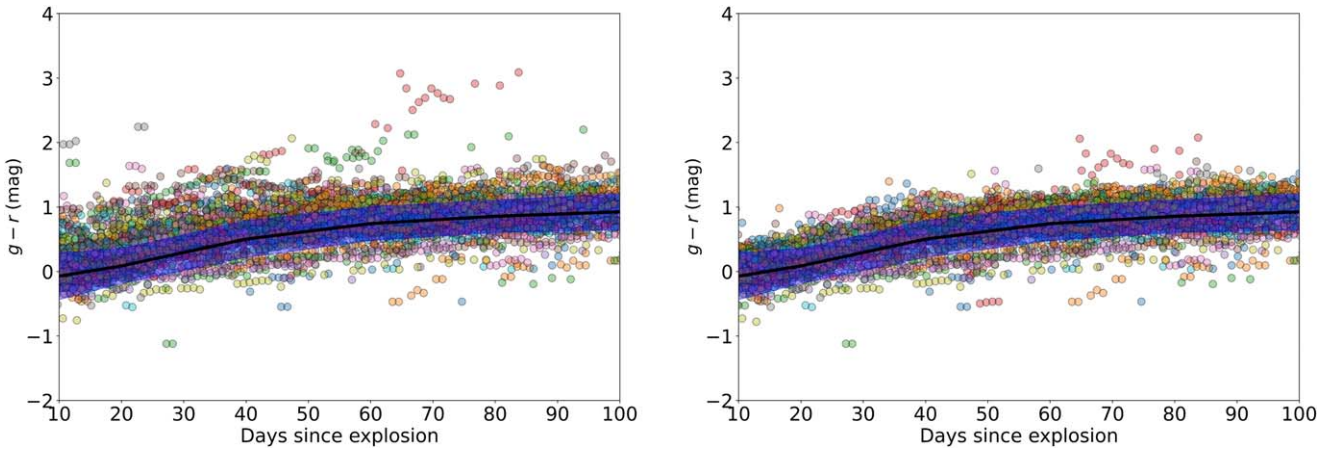

Figure 3. Left: The $g - r$ colors of the ZTF CLU Type II SN sample are shown in colored circles. The average color and standard deviation (1σ range) of the distribution, after filtering out SNe with Na I D EW > 1 Å, are shown by the black solid line and blue shaded region, respectively. Right: The sample $g - r$ color distribution after host-extinction correction. The color template is available in DOI:10.5281/zenodo.14538857.

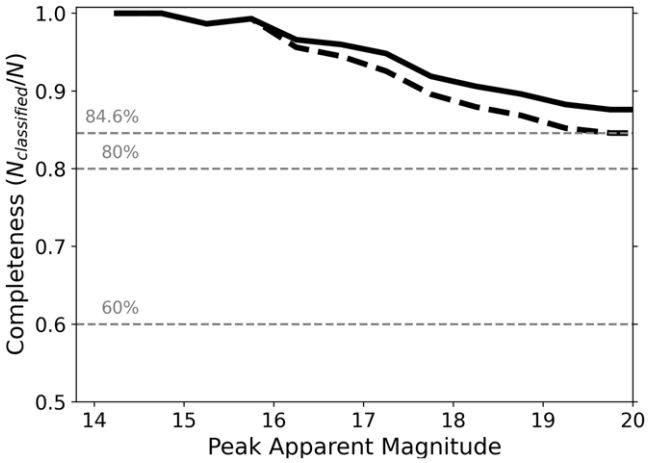

Figure 4. The cumulative distribution of the spectroscopic completeness of the ZTF CLU survey (with 2064 saved transients) as a function of peak r-band apparent magnitude. The dashed line accounts for the entire sample, whereas the solid black line omits 79 transients that are probably spurious. As a conservative lower limit, we consider the completeness depicted by the solid dashed line.

derived from the ZTF Bright Transient Survey (Fremling et al. 2020). We use the redshifts and WISE 3.36 μm absolute magnitudes (MW1) of the host galaxies of our sample and weight each event by $1/\mathrm{RCF}(z,\mathrm{MW1})$ to estimate the effect of galaxy catalog incompleteness (see Figure 10). This leads to an underestimate of the volumetric rate by $\approx$19%.

Finally, as mentioned earlier, the ZTF image subtraction pipeline has a reduced efficiency of the image subtraction algorithm on bright galaxy backgrounds and fainter targets. We weight each event by the inverse of the Pipeline Efficiency Factor ($1/\mathrm{PEF}(M, \mathrm{host})$). This leads to an underestimate of the rate by $\approx$6%.

Applying the corrections described above, we derive a corrected rate of $(3.9^{+0.4}_{-0.4}) \times 10^4\ \mathrm{Gpc^{-3}\ yr^{-1}}$ for Type IIP SNe and $(7.3^{+0.6}_{-0.6}) \times 10^3\ \mathrm{Gpc^{-3}\ yr^{-1}}$ for LLIIP SNe.

7. Discussion

7.1. Comparison to the Literature

The ZTF CLU sample of 330 SNe is the largest sample of Type IIP SNe from a systematic volume-limited survey to date. In Figure 11, we compare the luminosity function with the r-band Type II Luminosity functions from previous systematic SN surveys—62 Type II SNe from the Lick Observatory Supernova Survey Search (LOSS; Li et al. 2011), 21 Type II SNe from the Caltech Core-Collapse Project (CCCP; Arcavi et al. 2012), 50 Type II SNe from the Panoramic Survey Telescope and Rapid Response System (PS1; Sanders et al. 2015), 34 Type IIP SNe from the Sloan Digital Sky Survey II Supernova Survey (SDSS-II SNS; D'Andrea et al. 2010; Taylor et al. 2014). We also compare with the sample of 241 Type II SNe from the ZTF BTS used to analyze the rise-time properties of Type II SNe (K. Hinds et al. 2025, in preparation). In comparison with the LOSS sample, which is corrected for luminosity bias, we show the volume- and host-extinction corrected distribution in solid black and the volume-corrected but not host-extinction-corrected distribution in dashed violet. Our distribution without host extinction correction matches better with the LOSS luminosity function. In the comparison with the PS1 and CCCP samples, the CLU sample in dashed green is not corrected for luminosity bias. We note that the PS1 r-band sample was part of a flux-limited survey and the observed distribution follows what one

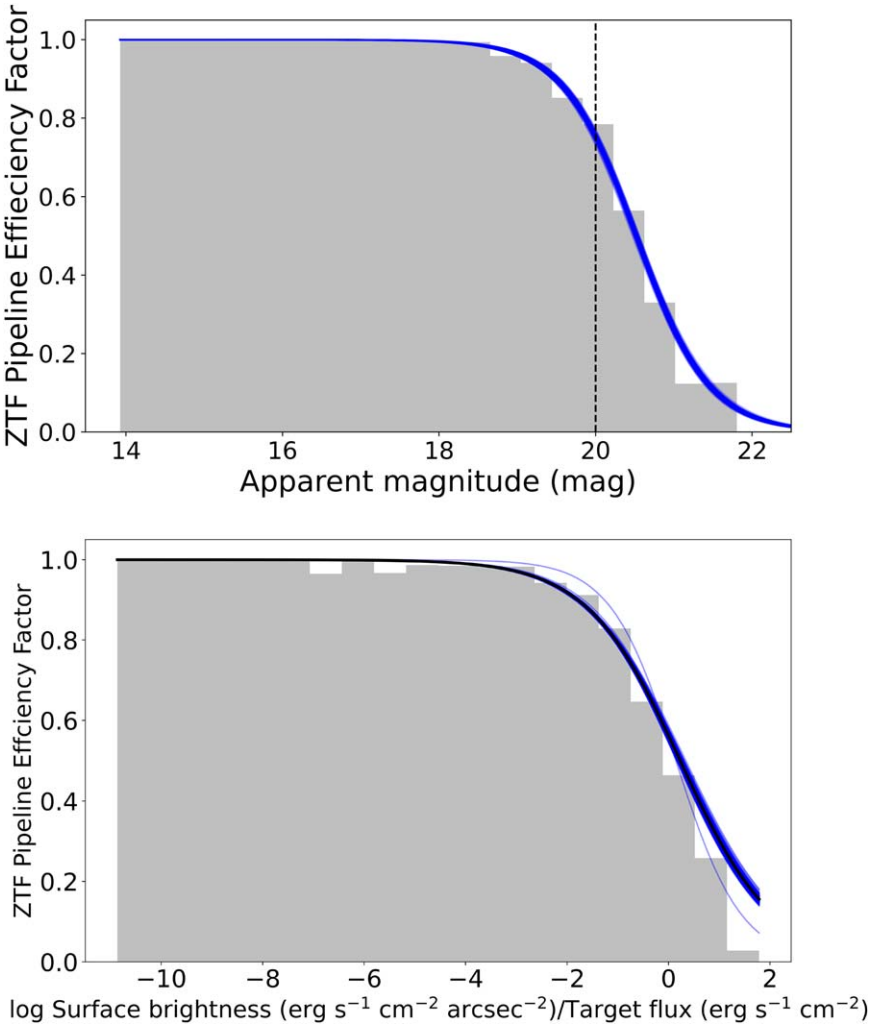

Figure 5. The ZTF pipeline recovery efficiency as a function of apparent magnitude (upper) and as a function of the ratio of local surface brightness and target flux (lower). The best-fit parameters of the logistic function is listed in Appendix C. The data required to reproduce the plot is available in DOI:10.5281/zenodo.14538857.

would typically expect without a volume correction. The CCCP experiment was also a flux-limited SN experiment. The observed CCCP distribution falls close to the mean and the fainter end of the dispersion of the ZTF CLU sample without any volume correction. The SDSS Type IIP SN sample from D'Andrea et al. (2010), which shows the *I*-band magnitude at 50 days post-explosion, does not have any SN fainter than −16 mag. The volume-corrected distribution of the peak *r*-band magnitude of the BTS Type II SN sample (K. Hinds et al. 2025, in preparation) in shaded green closely resembles the ZTF CLU distribution, with a higher fraction of fainter SNe in ZTF CLU sample without any volume correction (in orange), consistent with the experiment design.

We obtained a LLIIP fraction of 19^{+3}_{-4}% of the host-extinction corrected sample of CLU Type II SNe. The fraction of LLII SNe is ∼45% for the LOSS volume-corrected luminosity function without any host-extinction correction. The fraction of LLIIP in the raw PS1 and CCCP sample distribution is ∼3% and ∼9%, respectively.

The volumetric rate for Type II SNe from the LOSS survey was $(4.4^{+1.4}_{-1.4}) \times 10^4$ Gpc^{-3} yr^{-1}. Based on the LOSS survey statistics (Li et al. 2011), Type IIP SNe are 70% of all Type II SNe, thus the Type IIP SN rate is $\sim(3.1^{+1.0}_{-1.0})\times 10^4$ Gpc^{-3} yr^{-1}, which is consistent with the volumetric rate measured with the CLU sample. The Bright Transient Survey (BTS; Perley et al. 2022) and the Sloan Digital Sky Survey II Supernova Survey (SDSS-II SNS; Taylor et al. 2014) measured an overall core-collapse SN rate. BTS measured a CCSN rate of $(10.1^{+5.3}_{-3.5}) \times 10^4$ Gpc^{-3} yr^{-1}, and SDSS-II SNS measured a CCSN rate of $(10.6^{+1.9}_{-1.9}) \times 10^4$ Gpc^{-3} yr^{-1}. If we assume Type II SNe constitute 57% of all CCSNe and Type IIP SNe are 70% of all Type II SNe (Li et al. 2011), the Type IIP SN rates in

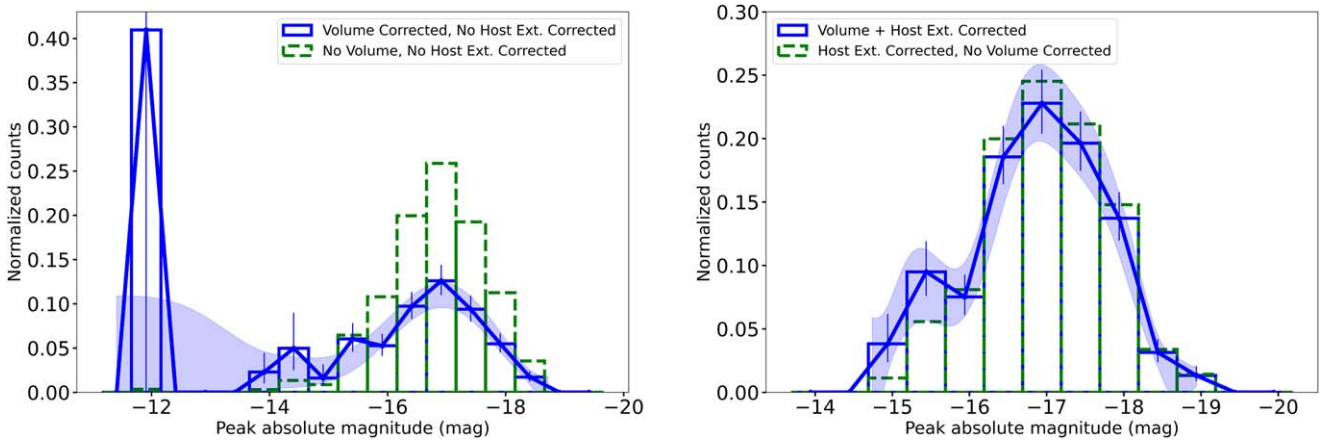

Figure 6. The peak *r*-band absolute magnitude distribution of the sample of 330 Type IIP SNe in CLU with Poisson errorbars before host-extinction correction (left) and after host-extinction correction (right). The volume-corrected luminosity function is shown in solid blue, while the raw distribution is shown in dashed green. GP fit is shown in blue. The luminosity function data is available in DOI:10.5281/zenodo.14538857.

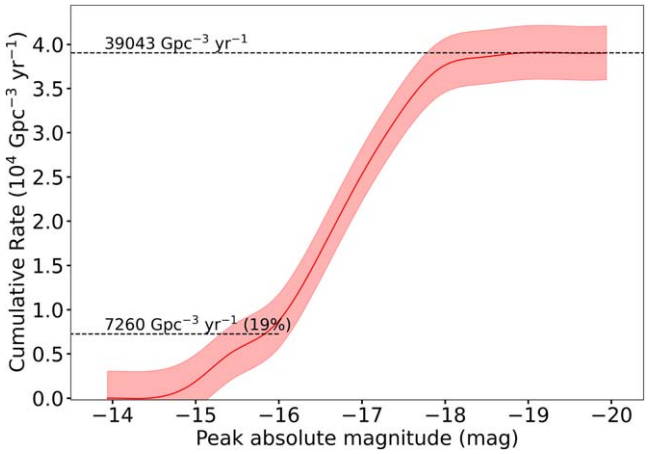

Figure 7. The cumulative distribution of the luminosity function of the ZTF CLU Type IIP sample. The IIP and LLIIP volumetric rates are shown by the horizontal dashed lines.

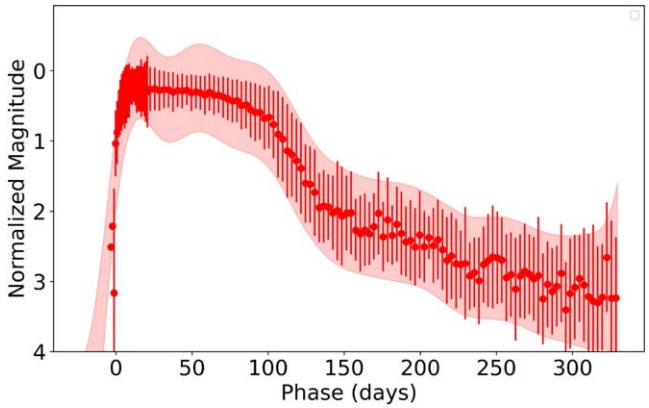

Figure 8. The *r*-band lightcurve template for Type IIP SNe. The solid points depict the mean lightcurve magnitudes of the ZTF CLU Type IIP sample. The line and shaded regions show the 1σ uncertainties derived from the GP fit.

BTS and SDSS-II would be $(4.0^{+2.1}_{-1.4}) \times 10^4\,\mathrm{Gpc^{-3}\,yr^{-1}}$ and $(4.2^{+0.8}_{-0.8}) \times 10^4\,\mathrm{Gpc^{-3}\,yr^{-1}}$ respectively, which is consistent with the ZTF CLU volumetric rate.

7.2. Can LLIIP SNe Account for the Fate of all 8–12 $\mathrm{M}_\odot$ *Stars?*

The fraction of massive stars that explode in this mass range is given by:

$$\frac{\int_{M_{\rm min}}^{12} \psi(M)\,dM}{\int_{M_{\rm min}}^{M_{\rm max}} \psi(M)\,dM},$$

where $M_{\rm min}$ is the minimum progenitor mass that explodes, $M_{\rm max}$ is the maximum progenitor mass of stars that explode, and $\psi(M) \propto M^{-2.35}$ for the Salpeter IMF. If we assume $M_{\rm max} = 40\,M_\odot$ and $M_{\rm min} = 8\,M_\odot$, 8–12 $M_\odot$ progenitors should account for 48% of all massive stars that collapse. If we assume $M_{\rm max} = 100\,M_\odot$ and $M_{\rm min} = 8\,M_\odot$, 8–12 $M_\odot$ progenitors account for 44% of all massive stars that explode. However, even though LLIIP SNe are the main observational candidates for low-mass CCSNe, we find that LLIIP SNe constitutes only 19^{+3}_{-4}% of all Type IIP SNe. If we assume that 40% of all CCSNe are Type IIP SNe (Li et al. 2011), LLIIP SNe are only 8^{+1}_{-2}% of all CCSNe. The mean local star formation rate density within $\sim$150 Mpc is $(17^{+7}_{-5}) \times 10^6\,M_\odot\,\mathrm{Gpc^{-3}\,yr^{-1}}$ (Horiuchi et al. 2011). This is also in good agreement with the local cosmic star formation rate (SFR) of $(18.5 \pm 1.20) \times 10^6\,M_\odot\,\mathrm{Gpc^{-3}\,yr^{-1}}$ (Hopkins & Beacom 2006). Assuming a SFR to SN rate conversion factor of 0.0088 (Horiuchi et al. 2011), the local SN rate would be $\approx 14 \times 10^4\,\mathrm{yr^{-1}\,Gpc^{-3}}$. Assuming a Salpeter IMF,

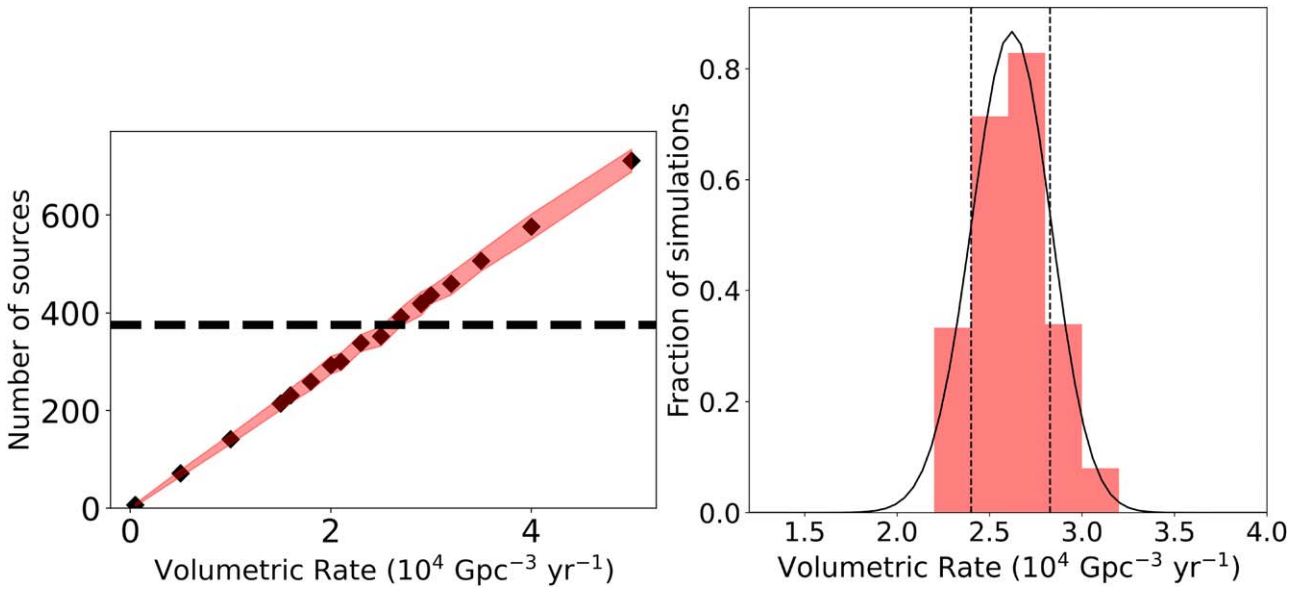

Figure 9. Left: The plot shows the number of LLIIP SNe that satisfy the filtering criteria as a function of the volumetric rate. The data points and the shaded region indicate the mean and standard deviation of detected transients, derived from 30 iterations of the simulated survey for each input volumetric rate. The dashed black line represents the observed number of Type IIP SNe in the ZTF CLU sample. Right: The fraction of simulations yielding the observed number of transients (within a 10% margin) is plotted against the volumetric rate.

the expected SN rate for 8–12 $M_\odot$ is $\approx 6.7 \times 10^4\,\mathrm{yr}^{-1}\,\mathrm{Gpc}^{-3}$, which is more than a factor of $9.2^{+0.8}_{-0.7}$ higher than the ZTF CLU LLIIP SN rate. How can this inconsistency be accounted for?

Observational bias. A possible dominant effect is that many SNe are missed because they are too faint for current optical surveys. We can rule out that faint IIP SN (>-14.5 mag) account for the missing SNe population as they account for $<1.5\%$ of the entire Type IIP SNe population. However, we note that ZTF CLU is sensitive to only 25 Mpc for potential SNe fainter than -12 mag and up to 40 Mpc for potential SNe fainter than -13 mag. If Type IIP SNe alone were the fate of all progenitors in this mass range, we require that all Type IIP SN fainter than ~ -18 mag originate from this progenitor mass range. The ZAMS mass for the entire sample will be estimated in Papers II and III. The other scenario is that current optical transient surveys like CLU might be missing a significant fraction of low-mass explosions due to extinction (e.g., see Jencson et al. 2019b; Fox et al. 2021). Mattila et al. (2012) estimate that locally $18.9^{+19.2}_{-9.5}\%$ of the CCSNe are missed by optical surveys. Jencson et al. (2019b) predict an even higher fraction, that $38.5^{+26.0}_{-21.9}\%$ of the CCSNe are missed by optical surveys. Jencson et al. (2019b) speculate that the objects SPIRITS16ix and SPIRITS16tn may represent a class of low-energy CCSNe arising preferentially in particularly extinguished environments. SPIRITS16tn is consistent with a LLIIP SN, heavily obscured by $A_V = 7$–9 mag. Another source of observational bias against LLIIP SNe could be the CLU galaxy catalog, if LLIIP SNe preferentially occurs in small galaxies.

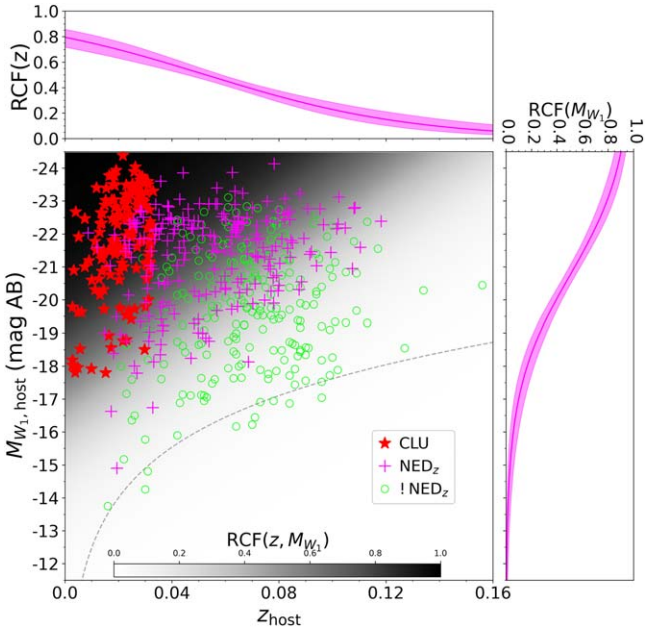

Figure 10. The redshift completeness factor of the galaxy catalogs as a function of the host redshift and W1-band magnitude, measured in Fremling et al. (2020). The red stars depict the hosts of the SNe of the CLU Type IIP sample.

Explode as Other Classes of Transients. We know that the majority ($\sim$70%) of young massive stars live in interacting binary systems and the outer envelopes of $\sim$33% of massive stars are stripped (e.g., see Sana et al. 2012). Thus, it is possible

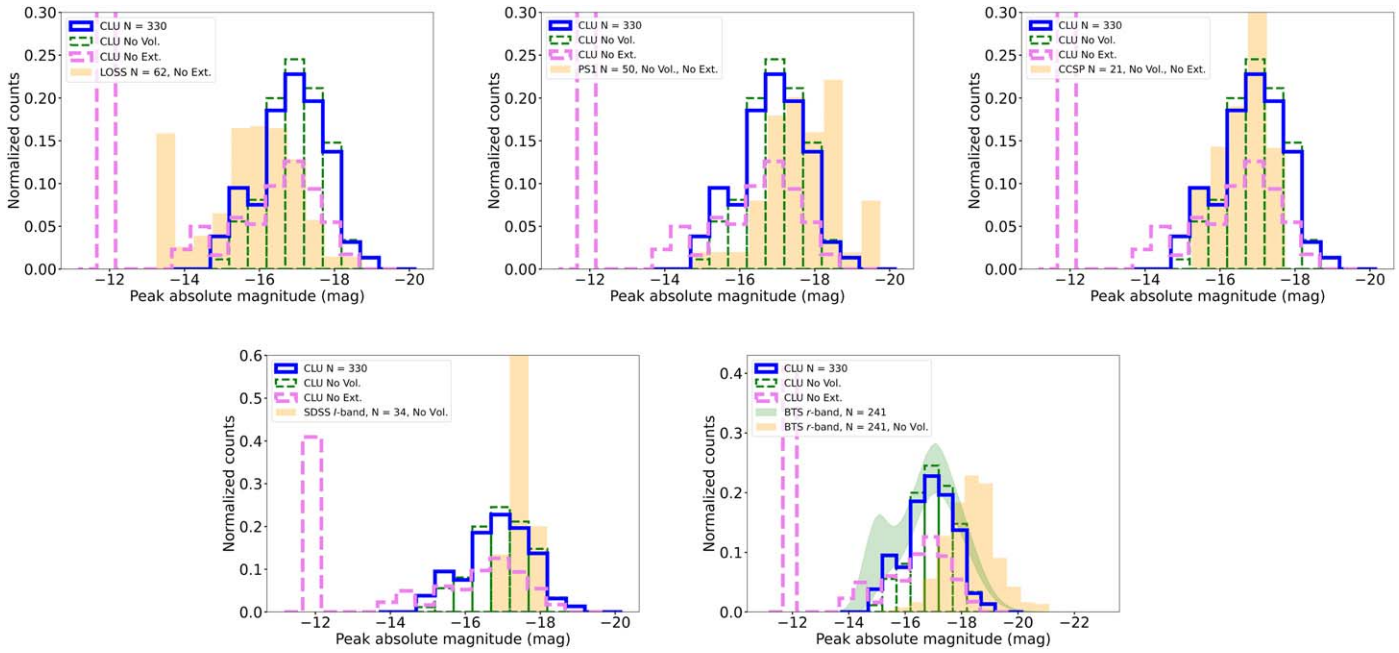

Figure 11. Comparison of the ZTF CLU Type II SNe luminosity function in *r*-band with the LOSS (*r*-band), PS1 (*r*-band), CCCP (*r*-band), SDSS (*I*-band), BTS (*r*-band) surveys (in shaded orange or green). The blue, green, and purple line depicts the volume and host-extinction corrected, only host-extinction corrected and only volume corrected distribution of the CLU Type IIP SNe sample, respectively.

that a significant fraction of 8–12 $M_{\odot}$ stars explode as stripped-envelope SNe in binary star systems. These stars with low-mass iron cores produce a low amount of Ni and ejecta mass (Moriya et al. 2017; Stockinger et al. 2020; Sandoval et al. 2021; Sawada et al. 2022; Burrows et al. 2024). Candidates for low nickel mass stripped-envelope SNe include double-peaked Type Ibc SNe such as SN 2021inl (Jacobson-Galán et al. 2022; Das et al. 2024b), rapidly evolving Type IIb SNe with a half-life of less than 10 days (e.g., Das et al. 2023; Ho et al. 2023; C. Fremling et al. 2025, in preparation), ultra-stripped SNe such as SN 2023zaw (Das et al. 2024a; Moore et al. 2025). Moore et al. (2025) measured a volumetric rate of rapidly evolving SESNe of $\approx(2.5^{+2.5}_{-1.4} \pm 0.9) \times 10^3\,\mathrm{Gpc^{-3}\,yr^{-1}}$, which is only ≈5% of the Type IIP SN rate. A systematic study of the lowest-nickel mass stripped-envelope SNe in CLU, including their rates and the nickel mass distribution will be explored in a future work. Also, ∼7–9 $M_{\odot}$ sAGB stars are predicted to undergo electron-capture SNe (Nomoto 1984), which could be the origin of the class of Intermediate Luminosity Red Transients (ILRTs) (e.g., AT 2019abn, NGC 300 2008OT-1, SN 2008S; Botticella et al. 2009; Adams et al. 2016; Jencson et al. 2019a; Rose et al. 2025; Valerin et al. 2025). Observations indicate that ILRTs comprise 1%–10% of the overall CCSNe rate (Thompson et al. 2009; Cai et al. 2021; Karambelkar et al. 2023).

Stellar Evolution and Explosion Models. The third explanation could be our limited theoretical understanding regarding the evolution and fate of 8–12 $M_{\odot}$ progenitors. Stars in this mass range have a qualitatively different core structure than at >12 $M_{\odot}$, with significantly lower compactness (Sukhbold et al. 2016). Their evolution is significantly more complex to model due to degeneracy effects. They develop thermal pulses that are numerically challenging to follow. Due to the steeply falling nature of the IMF, the lower mass limit $M_{\rm min}$ strongly affects the fraction of massive stars that explode. For example, if $M_{\rm min} = 9.7\,M_{\odot}$, then the fraction of massive stars <12 $M_{\odot}$ is ∼25%. To match the observed rate of LLIIP SNe, we require a minimum progenitor mass of $M_{\rm min} = 11.3^{+0.6}_{-0.7}\,M_{\odot}$. The low rate of LLIIP SNe can be reasonably explained if a fraction of potential progenitors within this mass range either fail to undergo Fe-core collapse or do not successfully explode. This outcome is plausible if their cores fail to achieve the necessary physical conditions for core collapse. Another possibility in binary stellar evolution is stellar mergers. Sana et al. (2012) predict that more than half of the progenitors of Type II SNe are merged stars or binary mass gainers. Thus, if single stars in the 8–12 $M_{\odot}$ merge, then we might instead observe the SN explosions of these progenitors that have a higher mass and undergo more luminous explosions (Zapartas et al. 2019, 2021).

It is likely that one or more of the above factors play a role in explaining the fate of all the lowest-mass stars that undergo core collapse.

8. Summary

In summary, we present the largest sample of 330 Type IIP SNe to derive the luminosity function to-date from a spectroscopic complete volume-limited SN survey. The sample is particularly critical to understand the low-luminosity population of CCSNe, with the sample of 36 LLIIP SNe ($M_{r,\mathrm{peak}} \geqslant -16$ mag) tripling the sample of LLIIP SNe in the literature. The key takeaways from the analysis are:

1. The luminosity function peaks at -17 mag and does not show a significant population >-14.5 mag, accounting for $< 1.5\%$ of all Type IIP SNe. The fraction of LLIIP SNe is $19^{+3}_{-4}\%$ of the Type IIP SNe population and $8^{+1}_{-2}\%$ of the CCSN population (see Figure 6).
2. We model the efficiency of the ZTF subtraction pipeline as a function of the alert flux and the ratio of background surface brightness to target flux. As expected, the recovery efficiency decreases as this ratio increases. The best-fit efficiency is $\sim$50% when the host surface brightness and target fluxes are comparable. Similarly, the best-fit efficiency decreases with an increase in target alert apparent magnitude and is $\approx$80% when the target magnitude is 20 mag (see Figure 5).
3. We derive a volumetric rate of $(3.9^{+0.4}_{-0.4}) \times 10^4\,\mathrm{Gpc^{-3}\,yr^{-1}}$ for Type IIP SNe and $(7.3^{+0.6}_{-0.6}) \times 10^3\,\mathrm{Gpc^{-3}\,yr^{-1}}$ for LLIIP SNe (see Figures 7, 9).
4. The expected SN rate for 8–12 $M_\odot$ is $\approx 6.7 \times 10^4\,\mathrm{yr^{-1}\,Gpc^{-3}}$, which is more than a factor of $9.2^{+0.8}_{-0.7}$ higher than the ZTF CLU LLIIP SNe rate. While LLIIP SNe represent the explosions of the lowest massive stars that explode, they cannot account for all 8–12 $M_\odot$ progenitors.

The robust LLIIP rate measured in this work shows a significant discrepancy between the calculated and predicted volumetric rates of SNe in the low mass-end (8–12 $M_\odot$) of core-collapse SNe. Future deep surveys such as the Legacy Survey of Space and Time (LSST; Ivezić et al. 2008) in synergy with high-cadenced surveys of ZTF could reveal a hidden population of $\geqslant -13$ mag CCSNe. To enhance the efficiency of spectroscopic completeness for faint SNe, we will conduct the ZTF Complete Astronomical Transient Survey within 150 Mpc (CATS150; Das et al. 2025). CATS150 will utilize the high efficiency of the Next Generation Palomar Spectrograph on the Palomar 200 inch Hale Telescope to achieve spectroscopic completeness exceeding 95% for even the faintest SNe. Also, SN survey in the local universe carried out at longer wavelengths by ground-based surveys such as the Wide-field Infrared Transient Explorer (WINTER; N. P. Lourie et al. 2020), Dynamic REd All-sky Monitoring Survey (DREAMS; Soon et al. 2020), Prime-focus Infrared Microlensing Experiment (PRIME; Kondo et al. 2023), Cryoscope and space-based telescopes such as the `Nancy Grace Roman Space Telescope` will be critical in constraining the missing SN population due to dust obscuration.

Acknowledgments

We thank the anonymous referee for their constructive feedback, which helped improve the quality of this manuscript.

Based on observations obtained with the Samuel Oschin Telescope 48 inch and the 60 inch Telescope at the Palomar Observatory as part of the Zwicky Transient Facility project. ZTF is supported by the National Science Foundation under grants No. AST-1440341 and AST-2034437 and a collaboration including current partners Caltech, IPAC, the Oskar Klein Center at Stockholm University, the University of Maryland, University of California, Berkeley, the University of Wisconsin at Milwaukee, University of Warwick, Ruhr University Bochum, Cornell University, Northwestern University and Drexel University. Operations are conducted by COO, IPAC, and UW.

Zwicky Transient Facility access for N.R., A.A.M., S.S., and C.L. was supported by Northwestern University and the Center for Interdisciplinary Exploration and Research in Astrophysics (CIERA). N.R., C.L., and A.A.M. are supported by DoE award #DE-SC0025599.

S.S. is partially supported by LBNL Subcontract 7707915.

SED Machine is based upon work supported by the National Science Foundation under grant No. 1106171.

The ZTF forced-photometry service was funded under the Heising-Simons Foundation grant #12540303 (PI: Graham).

The Gordon and Betty Moore Foundation, through both the Data-Driven Investigator Program and a dedicated grant, provided critical funding for SkyPortal.

This research has made use of the NASA/IPAC Extragalactic Database (NED), which is funded by the National Aeronautics and Space Administration and operated by the California Institute of Technology.

The Liverpool Telescope is operated on the island of La Palma by Liverpool John Moores University in the Spanish Observatorio del Roque de los Muchachos of the Instituto de Astrofisica de Canarias with financial support from the UK Science and Technology Facilities Council.

The W. M. Keck Observatory is operated as a scientific partnership among the California Institute of Technology, the University of California and the National Aeronautics and Space Administration. The Observatory was made possible by the generous financial support of the W. M. Keck Foundation. The authors wish to recognize and acknowledge the very significant cultural role and reverence that the summit of Maunakea has always had within the indigenous Hawaiian community. We are most fortunate to have the opportunity to conduct observations from this mountain.

Data Availability

All the photometric and spectroscopic data of the SNe in the sample will be made available on WISEREP and Zenodo after publication. The meta-data of the sample, extinction template, and pipeline recovery efficiency are available as a machine-readable tables in DOI:10.5281/zenodo.14538857.

Appendix A
Progenitor Mass from Pre-explosion Images versus SN Peak Magnitude

Here, we show the distribution of the Zero-Age Main-Sequence (ZAMS) mass estimated for Type II SNe from pre-explosion images. We can see that all LLIIP SNe have progenitor mass estimates of less than $<11\,M_{\odot}$ while SNe brighter than -16 mag have more massive progenitors. The SNe shown here are: SN 2003gd (Maund & Smartt 2009; Smartt 2015), SN 2005cs (Maund et al. 2014; Smartt 2015), SN 2009md (Fraser et al. 2011; Smartt 2015), SN 2006my (Maund et al. 2014; Smartt 2015), SN 2012A (Tomasella et al. 2013; Smartt 2015), SN 2013ej (Fraser et al. 2014; Smartt 2015), SN 2004et (Crockett et al. 2011; Smartt 2015), SN 2008bk (Maund et al. 2014; Smartt 2015), SN 2004A (Maund et al. 2014; Smartt 2015), SN 2012aw (Kochanek et al. 2012; Smartt 2015), SN 2009hd (Elias-Rosa et al. 2011; Smartt 2015), SN 2009kr (Fraser et al. 2010; Smartt 2015), SN 2012ec (Maund et al. 2013; Smartt 2015), SN 2018aoq (O'Neill et al. 2019), SN 2022acko (Van Dyk et al. 2023). A positive correlation between progenitor luminosity and V-band magnitude at 50 days since explosion is also reported in Rodríguez (2022).

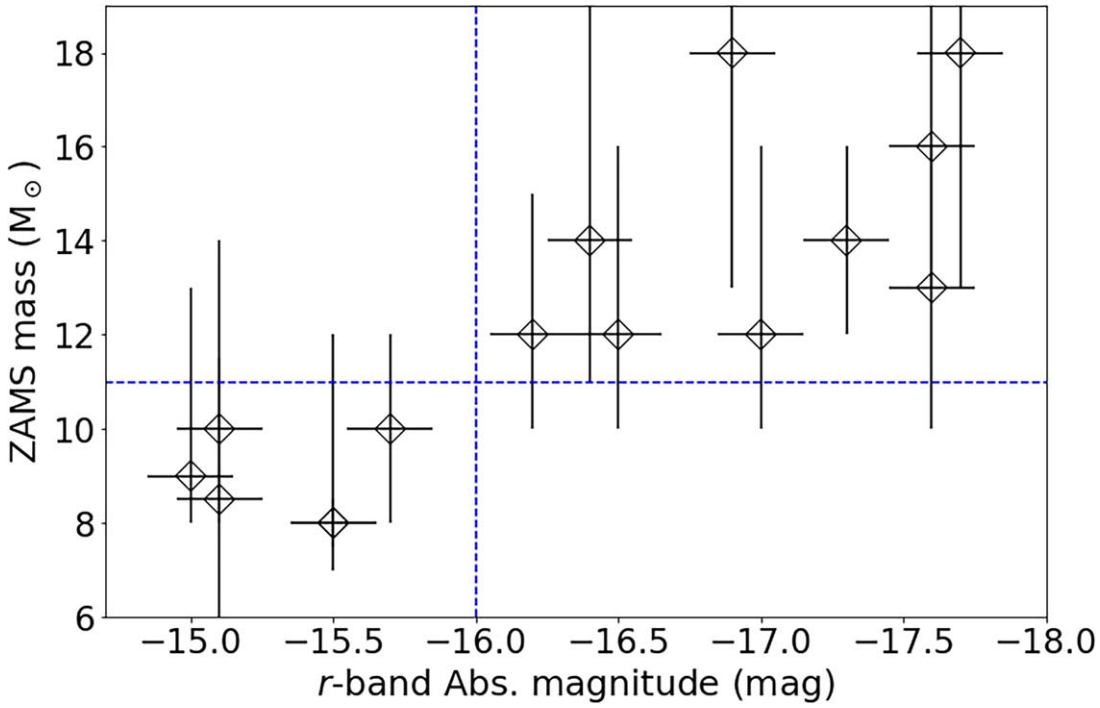

Figure 12. The distribution of the Zero-Age Main-Sequence (ZAMS) mass estimated for Type II SNe from pre-explosion images as a function of the peak r-band magnitude.

Appendix B
Distance Correction for Nearby Galaxies

Table B1 lists the distance measurements used for galaxies closer than 25 Mpc. We correct for the Virgo, Great Attractor, and Shapley supercluster infall based on the NASA Extragalactic Database object page (NED;[25] G. Helou et al. 1991).

Table B1
Distance Measurements Used for Galaxies <25 Mpc

Name	Distance (Mpc)
SN 2021gmj/ZTF21aaqgmjt[a]	13.10
SN 2022acko/ZTF22abyivoq[b]	23.40
SN 2023axu/ZTF23aabngtm[c]	13.68
SN 2023hlf/ZTF23aaitpjv[d]	9.54
SN 2022aagp/ZTF22abtspsw[d]	25.15
SN 2023ijd/ZTF23aajrmfh[d]	14.94
SN 2022jzc/ZTF22aakdbia[d]	19.64

Notes.
[a] Valerin et al. (2022).
[b] Van Dyk et al. (2023).
[c] Shrestha et al. (2024).
[d] G. Helou et al. (1991).

Appendix C
ZTF Pipeline Recovery Efficiency Fits

The corner plot for the MCMC fit to

$$p(m) = \frac{1}{1 + \exp(a(m - c))},$$

where m is the alert apparent magnitude is shown in Figure 13. The best-fit values are $a = 2.28^{+0.03}_{-0.04}$ and $c = 20.57^{+0.01}_{-0.01}$.

The corner plot for the MCMC fit to

$$p(r) = \frac{1}{1 + \exp(a(r - c))},$$

where r is the ratio of the alert apparent magnitude to the local surface brightness is shown in Figure 13. The best-fit values are $a = 1.12^{+0.02}_{-0.02}$ and $c = 0.21^{+0.03}_{-0.03}$.

[25] https://ned.ipac.caltech.edu/

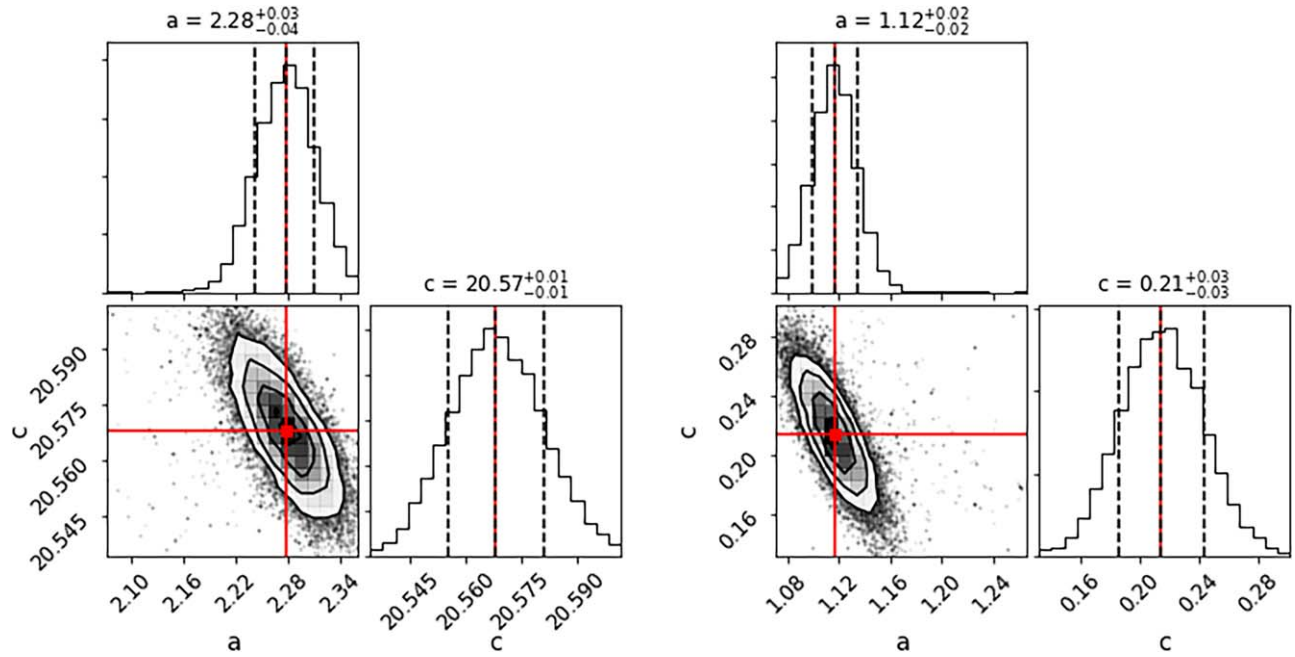

Figure 13. Corner plots for the logistic function fit to the pipeline efficiency as a function of apparent magnitude (left) and the ratio of the alert apparent magnitude to the local surface brightness (right).

Appendix D
Sample of CLU Type II SNe

The full version of the sample summary table is shown in Table D1.

Table D1
Summary Table of the CLU Type II SN Sample

Name	R.A. (hh:mm:ss)	Decl. (dd:mm:ss)	Redshift	t_{expl} (MJD)	1st Detection (MJD)	Peak mag$_r$ (mag)	$A_{V,MW}$ (mag)	$A_{V,host}$ (mag)
ZTF18aaegvyd/SN 2019env	09:09:35.63	+29:58:14.4	0.024	58606.7	58608.2	−17.03	0.07	0.00
ZTF18aaqkywr/SN 2022giv	12:23:14.92	+51:11:28.3	0.031	59655.9	59670.4	−16.77	0.05	0.00
ZTF18aaqpowv/SN 2024iwm	11:28:17.83	+26:58:26.37	0.032	60443.2	60444.2	−17.42	0.05	0.00
ZTF18aaszvfn/SN 2021iaw	14:23:07.88	+50:13:14.9	0.027	59306.4	59307.3	−16.77	0.06	0.00
ZTF18aawgrxz/SN 2021lmp	15:04:17.64	+48:55:10.7	0.027	59338.9	59339.3	−16.85	0.04	0.42
ZTF18aaxzlmy/SN 2018lrq	13:34:51.37	+34:03:20.5	0.025	58218.8	58219.3	−16.62	0.03	0.99
ZTF18abbpxik/SN 2018cqp	15:22:50.32	+08:04:49.1	0.032	58282.7	58283.2	−18.08	0.10	0.71
ZTF18abbpyvk/SN 2018cqi	13:57:40.91	+17:30:29.1	0.022	58284.7	58286.2	−18.29	0.09	0.07
ZTF18abcpmwh/SN 2018cur	12:59:09.12	+37:19:00.1	0.015	58289.7	58291.2	−17.56	0.04	0.00
ZTF18abdbysy/SN 2018cyg	15:34:08.48	+56:41:48.6	0.011	58294.8	58295.2	−17.08	0.05	2.05
ZTF18abdfwcy/SN 2018cwa	12:42:43.85	+34:06:26.3	0.014	58290.8	58295.2	−17.27	0.05	0.00
ZTF18abdjmfh/SN 2018dct	16:15:08.80	+26:33:36.2	0.030	58298.8	58300.3	−18.72	0.12	1.27
ZTF18abjkryl/SN 2018dzc	18:23:09.26	+21:14:56.4	0.010	58308.4	58308.4	−16.30	0.48	0.49
ZTF18abjndhh/SN 2018ecj	11:32:43.02	+62:25:57.9	0.013	58322.2	58324.2	−17.03	0.03	1.34
ZTF18abjovdz/SN 2018dht	20:55:19.05	+00:32:18.6	0.024	58309.9	58312.4	−18.36	0.23	1.48
ZTF18abklbam/SN 2018elp	14:31:19.10	+21:17:24.7	0.031	58329.2	58331.2	−18.00	0.13	0.00
ZTF18abmdpwe/SN 2018evy	18:22:38.17	+15:41:47.6	0.018	58339.2	58340.2	−18.06	0.54	0.00
ZTF18abnxfve/SN 2018lrz	22:29:52.72	+36:43:50.1	0.025	58347.8	58349.3	−15.94	0.30	0.00
ZTF18abokyfk/SN 2018fif	00:09:26.55	+47:21:14.7	0.017	58350.8	58351.4	−17.12	0.30	0.00
ZTF18abrpkdw/SN 2018lsa	21:45:07.20	+15:35:09.0	0.031	58355.8	58357.2	−16.49	0.29	0.00

Table D1
(Continued)

Name	R.A. (hh:mm:ss)	Decl. (dd:mm:ss)	Redshift	$t_{\rm expl}$ (MJD)	1st Detection (MJD)	Peak mag$_r$ (mag)	$A_{V,\rm MW}$ (mag)	$A_{V,\rm host}$ (mag)
ZTF18abrzbtb/SN 2018ggu	07:43:04.67	+50:17:22.2	0.019	59120.0	59120.5	−15.66	0.19	0.00
ZTF18abvmlow/SN 2018lcd	01:51:10.65	−03:29:24.9	0.017	58479.2	58483.2	−18.02	0.08	0.00
ZTF18abvvmdf/SN 2018gts	16:36:47.39	+55:44:08.8	0.030	58373.2	58374.2	−18.02	0.05	0.92
ZTF18abwisaz/SN 2024kan	22:49:07.02	+32:47:53.12	0.028	60454.5	60456.4	−17.45	0.36	0.00
ZTF18abxbmcl/SN 2018hcp	08:22:57.66	+27:42:10.5	0.020	58377.0	58378.5	−19.19	0.10	2.05
ZTF18abzrgim/SN 2018gvt	23:07:32.54	+23:00:20.9	0.021	58386.8	58388.3	−17.49	0.63	0.00
ZTF18acbvhit/SN 2018hle	03:39:28.11	−13:07:02.4	0.014	58418.7	58422.4	−16.80	0.15	0.21
ZTF18aceqrcy/SN 2018joy	10:19:40.32	+12:50:37.7	0.032	58428.0	58429.5	−17.77	0.18	0.99
ZTF18acrflch/SN 2018jgy	03:06:59.88	−06:45:14.0	0.029	58445.8	58448.3	−17.38	0.23	0.00
ZTF18acrkaks/SN 2018jwq	05:17:54.17	+08:54:51.3	0.030	58438.4	58439.4	−16.51	0.93	0.00
ZTF18acrtvmm/SN 2018jfp	03:17:56.27	−00:10:10.7	0.023	58448.8	58450.3	−17.55	0.20	0.00
ZTF18acsxkov/SN 2018kds	00:10:09.06	−04:42:33.2	0.030	58449.7	58456.2	−16.68	0.09	0.00
ZTF18acurdnh/SN 2018jvr	10:07:20.35	+04:04:49.2	0.029	58458.5	58461.5	−16.38	0.05	0.00
ZTF18acurqaw/SN 2018hwm	08:21:28.20	+03:09:52.3	0.009	58432.5	58441.4	−17.05	0.07	3.39
ZTF18acyybvg/SN 2018kkv	11:34:33.85	+22:31:09.2	0.032	58470.5	58471.5	−16.69	0.06	0.00
ZTF18adachwf/SN 2018lev	15:13:08.16	+41:15:49.2	0.029	58472.2	58475.5	−16.94	0.06	0.14
ZTF18adazblo/SN 2018ldu	09:09:32.49	+20:24:25.1	0.027	58476.4	58480.4	−16.67	0.11	0.00
ZTF18adbclkd/SN 2018kpo	03:40:43.06	−06:25:23.9	0.017	58478.3	58481.3	−17.28	0.15	0.00
ZTF19aaabzpt/SN 2018lab	06:16:26.51	−21:22:32.4	0.009	58479.3	58487.3	−15.81	0.24	0.71
ZTF19aadnxnl/SN 2019va	13:35:14.68	+44:45:58.6	0.009	58498.5	58502.5	−16.87	0.05	0.00
ZTF19aadnxog/SN 2019vb	13:14:23.07	+30:29:06.6	0.020	58498.5	58503.5	−18.04	0.04	0.00
ZTF19aailepg/SN 2019amt	11:17:52.25	+30:09:23.5	0.030	58518.4	58522.4	−17.11	0.05	0.00
ZTF19aajwkbb/SN 2019bsw	10:05:06.10	−16:24:21.3	0.027	58502.5	58511.4	−16.75	0.14	0.00
ZTF19aaklqoi/SN 2021adnr	08:57:54.94	+20:07:12.6	0.031	59514.0	59518.5	−17.27	0.08	1.20
ZTF19aakpxfm/SN 2019aor	07:24:57.85	−27:31:53.7	0.025	58476.4	58476.4	−17.94	0.83	0.00
ZTF19aalycsv/SN 2019txj	10:48:39.19	+76:48:05.3	0.023	58543.3	58546.2	−15.27	0.07	0.00
ZTF19aamftfu/SN 2019cag	02:23:21.52	+53:23:41.3	0.025	58551.6	58556.1	−17.30	0.53	0.00
ZTF19aamwhat/SN 2019bzd	14:47:32.03	−19:45:57.7	0.008	58559.7	58568.4	−15.83	0.24	0.07
ZTF19aanfnvl/SN 2019crk	10:10:31.69	+10:02:37.0	0.032	58561.7	58567.2	−17.77	0.12	0.00
ZTF19aanhhal/SN 2019cec	13:41:40.74	+55:40:10.7	0.026	58561.9	58562.3	−17.23	0.03	0.00
ZTF19aaniore/SN 2019ceg	16:27:51.64	+62:41:32.5	0.030	58564.5	58567.5	−17.31	0.09	0.00
ZTF19aanqzle/SN 2019cmm	11:18:07.29	+75:08:50.8	0.023	58570.2	58572.2	−16.03	0.16	0.00
ZTF19aanrrqu/SN 2019clp	12:13:39.83	+16:07:24.4	0.024	58569.8	58572.3	−18.02	0.10	0.00
ZTF19aapafit/SN 2019cvz	16:30:54.08	+46:35:18.4	0.019	58576.5	58577.4	−17.05	0.04	0.00
ZTF19aaqxosb/SN 2019dok	13:46:51.76	+16:16:53.7	0.019	58588.3	58589.2	−16.64	0.07	0.00
ZTF19aarjfqe/SN 2019dvd	12:31:06.89	+00:27:54.6	0.021	58592.8	58596.3	−16.93	0.06	0.00
ZTF19aarykkb/SN 2019dzk	17:13:21.95	−09:57:52.1	0.024	58595.4	58598.3	−18.17	1.54	0.00
ZTF19aatmadu/SN 2019esn	14:51:56.11	+51:15:51.2	0.027	58602.4	58605.4	−16.00	0.06	0.00
ZTF19aauishy/SN 2019evl	13:31:01.26	+34:09:12.5	0.023	58609.3	58612.2	−16.45	0.03	0.00
ZTF19aavrcew/SN 2019fyw	13:07:18.44	+02:00:11.5	0.019	58625.2	58633.2	−17.78	0.08	0.00
ZTF19aavtcjs/SN 2019gss	15:24:44.44	+68:43:44.3	0.022	58630.3	58633.3	−17.89	0.07	2.19
ZTF19aawgxdn/SN 2019gmh	16:31:03.16	+41:09:14.2	0.031	58634.3	58635.2	−17.39	0.03	0.00
ZTF19aaykqsk/SN 2019hci	11:16:03.35	−00:31:55.9	0.026	58641.7	58643.2	−17.02	0.17	0.00
ZTF19aayrosj/SN 2019hrb	20:54:12.08	+10:33:01.1	0.015	58642.5	58644.5	−17.64	0.26	1.70
ZTF19aazudta/SN 2019hqm	17:36:56.18	+21:06:17.1	0.024	58648.8	58650.3	−16.98	0.23	0.00
ZTF19aazyvub/SN 2019hnl	23:43:10.25	−02:56:58.6	0.023	58649.5	58651.5	−17.13	0.09	0.00
ZTF19abaamsd/SN 2019ifm	17:23:41.33	+52:00:36.1	0.024	58652.8	58653.3	−17.33	0.09	0.00
ZTF19abajxet/SN 2019hyk	14:17:57.85	+26:25:17.6	0.015	58655.7	58657.2	−17.77	0.06	0.00
ZTF19abalqkq/SN 2019khq	17:50:41.76	+14:49:26.3	0.014	58645.9	58650.3	−15.76	0.26	1.63
ZTF19abbnamr/SN 2019iex	23:51:03.63	+20:08:43.7	0.014	58659.0	58660.5	−17.40	0.20	0.00
ZTF19abbwfgp/SN 2019ikb	17:13:17.71	+43:47:03.5	0.026	58660.8	58661.3	−18.16	0.05	0.00
ZTF19abctzkc/SN 2019tti	00:18:59.83	+08:46:28.2	0.019	58644.4	58646.4	−15.67	0.55	0.21
ZTF19abejaiy/SN 2019krp	14:07:33.70	+14:38:03.3	0.017	58670.2	58671.2	−15.45	0.04	0.00
ZTF19abjrjdw/SN 2019mkr	17:11:05.78	+05:51:07.3	0.022	58687.7	58689.2	−17.56	0.43	0.00
ZTF19abjsmmv/SN 2019mor	15:38:38.04	+36:57:31.0	0.019	58693.3	58694.2	−17.13	0.06	0.00

Table D1
(Continued)

Name	R.A. (hh:mm:ss)	Decl. (dd:mm:ss)	Redshift	$t_{\rm expl}$ (MJD)	1st Detection (MJD)	Peak mag$_r$ (mag)	$A_{V,\rm MW}$ (mag)	$A_{V,\rm host}$ (mag)
ZTF19ablfoqa/SN 2019tya	02:09:38.03	+01:33:06.7	0.032	58694.0	58694.5	−15.93	0.08	0.00
ZTF19abllxfy/SN 2019ttl	21:52:43.47	+38:56:00.8	0.020	58682.9	58690.3	−15.36	0.88	0.00
ZTF19abpyqog/SN 2019oba	19:57:03.47	+50:11:20.1	0.031	58708.3	58711.2	−17.22	0.40	0.00
ZTF19abqhobb/SN 2019nvm	17:25:38.66	+59:26:48.2	0.018	58713.7	58714.2	−17.59	0.08	0.00
ZTF19abqrhvt/SN 2019nyk	00:15:15.20	−08:11:21.8	0.021	58713.4	58715.4	−18.09	0.10	0.00
ZTF19abqrhvy/SN 2019odf	22:48:44.69	+27:34:18.5	0.032	58714.9	58715.4	−18.18	0.14	0.00
ZTF19abrnjwi/SN 2019omb	00:12:39.66	+05:30:32.0	0.028	58717.9	58719.4	−17.20	0.07	0.00
ZTF19abwztsb/SN 2019pjs	18:04:40.34	+21:38:04.2	0.007	58731.7	58734.2	−16.23	0.29	0.00
ZTF19abzmoov/SN 2019qba	15:37:44.70	+22:25:36.4	0.025	58735.6	58737.1	−16.68	0.12	0.00
ZTF19acalxgp/SN 2019qiq	23:44:56.09	−04:16:33.1	0.029	58735.4	58737.3	−15.86	0.12	0.00
ZTF19acblhxc/SN 2019rho	02:12:49.18	−06:42:05.9	0.017	58753.4	58756.4	−17.21	0.07	0.21
ZTF19acbpqlh/SN 2019rpn	21:19:41.19	+37:31:19.3	0.026	58709.8	58711.2	−16.28	0.46	0.00
ZTF19acbwejj/SN 2019upq	14:29:08.13	+27:27:00.6	0.014	58754.1	58758.1	−17.80	0.05	0.00
ZTF19acewuwn/SN 2019ssl	23:20:17.26	+35:29:35.3	0.027	58771.7	58772.2	−16.96	0.27	0.00
ZTF19acftfav/SN 2019ssi	23:30:56.12	+15:29:29.8	0.013	58773.7	58774.2	−16.51	0.19	0.00
ZTF19acgbkzr/SN 2019szo	00:19:56.64	+15:05:36.1	0.026	58774.8	58775.3	−16.73	0.13	0.00
ZTF19acgzwbm/SN 2019tba	04:55:09.84	−16:09:01.3	0.020	58770.5	58776.5	−16.34	0.18	0.00
ZTF19aclobbu/SN 2019twk	02:23:05.28	+46:52:56.7	0.018	58787.3	58788.3	−17.63	0.49	0.00
ZTF19acnphay/SN 2019ubr	06:25:52.32	+64:44:38.4	0.014	58769.5	58772.5	−16.57	0.32	2.40
ZTF19acrcxri/SN 2019ult	23:58:47.97	+14:44:31.3	0.027	58795.1	58797.1	−18.42	0.11	0.00
ZTF19acryurj/SN 2019ust	00:54:22.41	+31:40:12.6	0.022	58798.2	58800.3	−18.10	0.17	0.00
ZTF19actnwtn/SN 2019vdl	09:29:31.80	+44:25:20.0	0.025	58803.5	58804.5	−17.35	0.06	0.57
ZTF19actnyae/SN 2019vdm	11:26:24.51	+22:37:11.0	0.032	58804.0	58805.5	−16.88	0.04	0.00
ZTF19acvtrxj/SN 2019vjl	09:49:23.69	+01:08:46.6	0.025	58808.5	58812.6	−17.58	0.23	0.07
ZTF19acwrrvg/SN 2019vsr	02:01:57.73	+44:48:32.1	0.027	58816.7	58819.2	−18.66	0.21	0.00
ZTF19acxgwvo/SN 2019wbd	23:20:35.17	−00:52:51.0	0.015	58815.7	58820.2	−17.20	0.10	0.35
ZTF19acyjjni/SN 2019xbm	13:07:13.99	+58:08:03.3	0.028	58823.0	58831.6	−16.94	0.04	0.42
ZTF19acykzsk/SN 2019wqj	02:11:37.09	+34:02:28.7	0.021	58823.2	58827.2	−16.31	0.27	0.07
ZTF19acytcsg/SN 2019wvz	10:20:28.67	+50:28:04.5	0.032	58832.5	58833.4	−17.60	0.03	0.00
ZTF19adakmbh/SN 2019xgi	21:55:25.49	+34:30:37.8	0.018	58834.1	58837.1	−17.90	0.46	1.63
ZTF20aarenrz/SN 2021qyy	11:44:29.64	+69:43:45.4	0.009	59388.8	59390.2	−16.55	0.03	0.00
ZTF21aaabwem/SN 2020aeqx	13:13:00.02	+06:10:12.1	0.032	59211.0	59215.5	−16.79	0.10	0.00
ZTF21aaagypx/SN 2021V	11:13:07.92	+05:04:19.3	0.027	59213.4	59216.4	−17.43	0.20	0.00
ZTF21aabfwwl/SN 2021iy	11:18:31.68	−06:16:40.5	0.014	59217.9	59219.4	−15.55	0.14	0.00
ZTF21aabygea/SN 2021os	12:02:54.08	+05:36:53.1	0.019	59219.5	59221.4	−17.28	0.05	0.00
ZTF21aaeoqxf/SN 2021aek	11:59:48.02	−21:23:13.0	0.022	59225.5	59227.5	−17.61	0.13	0.00
ZTF21aaeqwov/SN 2021htp	07:43:04.75	+50:17:19.4	0.019	59119.0	59119.5	−16.39	0.19	0.00
ZTF21aafepon/SN 2021ass	01:50:10.12	+27:38:42.7	0.012	59230.6	59231.1	−16.24	0.23	0.07
ZTF21aafkwtk/SN 2021apg	13:41:19.24	+24:29:43.9	0.027	59229.5	59231.4	−16.98	0.03	0.00
ZTF21aagtqna/SN 2021brb	18:05:15.31	+46:52:56.0	0.023	59238.5	59248.5	−16.84	0.11	0.00
ZTF21aahgspm/SN 2021cah	02:48:30.72	+50:45:36.0	0.016	59250.7	59251.1	−17.43	0.98	0.00
ZTF21aaipypa/SN 2021cgu	11:03:03.71	+05:05:53.4	0.025	59252.4	59253.4	−18.34	0.10	0.00
ZTF21aakvroo/SN 2021cwe	15:45:31.20	+30:09:43.3	0.032	59257.0	59258.5	−17.11	0.09	0.00
ZTF21aaluqkp/SN 2021dhx	11:05:10.37	−15:21:10.1	0.025	59263.3	59264.3	−16.99	0.14	0.00
ZTF21aalxurx/SN 2021dqs	13:44:05.74	+43:04:18.0	0.027	59259.9	59264.4	−16.33	0.03	0.00
ZTF21aanjvng/SN 2021dvk	08:07:38.41	+08:56:24.2	0.030	59269.3	59271.2	−16.65	0.07	0.00
ZTF21aantsla/SN 2021ech	12:06:20.42	+37:00:47.1	0.021	59274.3	59275.2	−16.44	0.06	0.00
ZTF21aanzcuj/SN 2021enz	12:07:05.23	+42:59:18.3	0.024	59275.9	59276.3	−16.69	0.04	0.00
ZTF21aaobkmg/SN 2021eui	19:20:55.80	+43:07:14.6	0.015	59273.5	59276.5	−15.34	0.28	0.00
ZTF21aapkcmr/SN 2021fnj	14:23:42.67	+28:20:45.7	0.030	59285.4	59290.4	−17.91	0.05	0.42
ZTF21aapliyn/SN 2021foj	13:45:26.60	+47:55:05.3	0.028	59286.3	59291.3	−17.11	0.08	0.00
ZTF21aaqgmjt/SN 2021gmj	10:38:47.27	+53:30:30.3	0.003	59292.3	59293.2	−15.02	0.06	0.00
ZTF21aaqjmps/SN 2021gvm	13:30:01.22	+13:24:40.2	0.025	59292.8	59294.3	−18.10	0.07	0.00
ZTF21aaqldsj/SN 2021hac	14:12:30.45	+34:33:00.3	0.032	59293.3	59294.3	−16.95	0.04	0.00
ZTF21aaqugxm/SN 2021hdt	11:34:45.73	+42:57:55.3	0.019	59299.4	59300.3	−18.12	0.07	0.00

Table D1
(Continued)

Name	R.A. (hh:mm:ss)	Decl. (dd:mm:ss)	Redshift	$t_{\rm expl}$ (MJD)	1st Detection (MJD)	Peak mag$_r$ (mag)	$A_{V,\rm MW}$ (mag)	$A_{V,\rm host}$ (mag)
ZTF21aaqyifh/SN 2021hqe	09:41:30.96	+10:38:22.8	0.019	59297.3	59301.2	−16.86	0.06	0.71
ZTF21aaqyuun/SN 2021hkf	11:44:23.27	+08:10:41.4	0.019	59300.3	59302.3	−16.38	0.07	0.00
ZTF21aardvtn/SN 2021htp	07:43:04.76	+50:17:19.6	0.019	59119.0	59119.5	−16.42	0.19	0.00
ZTF21aasksnl/SN 2021mju	16:41:47.59	+19:21:53.5	0.028	59292.0	59301.4	−16.08	0.21	0.42
ZTF21aavhnpk/SN 2021jsf	20:50:21.44	+01:08:29.5	0.028	59313.0	59317.4	−17.33	0.29	0.00
ZTF21aaxtzzj/SN 2021kqj	11:04:58.16	+30:01:46.8	0.029	59331.8	59334.3	−17.72	0.07	1.41
ZTF21aazhegf/SN 2021llp	09:29:31.17	+25:33:25.0	0.033	59339.2	59340.2	−17.75	0.09	0.00
ZTF21abbomrf/SN 2020ghq	14:45:20.59	+38:44:18.5	0.015	59347.8	59349.2	−15.72	0.03	0.00
ZTF21abcacpa/SN 2021mtb	20:03:44.13	+49:59:34.7	0.027	59350.9	59353.4	−16.45	0.39	0.00
ZTF21abcmzvk/SN 2021nli	14:02:12.66	−18:45:16.1	0.030	59354.2	59356.2	−17.62	0.25	0.00
ZTF21abcpbqd/SN 2014gz	14:15:50.78	+01:52:57.4	0.026	59359.3	59359.3	−17.72	0.13	0.49
ZTF21abfiuqf/SN 2021pla	16:05:38.19	+69:35:41.2	0.024	59375.4	59376.3	−17.00	0.08	0.21
ZTF21abfjaxa/SN 2021pkh	12:48:41.97	+26:25:06.7	0.023	59372.2	59373.2	−17.43	0.03	2.05
ZTF21abfjdev/SN 2021pqj	11:05:35.47	+19:41:22.2	0.032	59366.2	59367.2	−16.99	0.07	0.00
ZTF21abfoytp/SN 2021pnh	15:50:50.63	+22:14:16.1	0.031	59373.8	59376.3	−16.68	0.17	0.49
ZTF21abgilzj/SN 2021qcr	17:10:21.60	−03:13:49.7	0.029	59289.0	59295.4	−18.12	1.14	0.00
ZTF21abglcxm/SN 2021qcs	15:29:22.82	−12:14:54.4	0.011	59377.3	59378.2	−15.65	0.43	0.42
ZTF21abhhrpj/SN 2021qiu	21:45:50.08	+15:11:01.3	0.029	59380.4	59381.4	−17.88	0.24	0.00
ZTF21abiblpl/SN 2021qzi	20:45:13.87	−05:37:09.9	0.027	59389.4	59391.3	−17.30	0.17	0.00
ZTF21abioeyq/SN 2021rhk	14:03:02.40	+08:45:56.4	0.023	59394.7	59395.2	−17.74	0.07	0.00
ZTF21abjcjmc/SN 2021skn	16:24:49.00	+39:44:04.7	0.030	59398.3	59399.2	−18.02	0.03	0.00
ZTF21abjcliz/SN 2021skm	16:16:56.05	+21:48:35.8	0.031	59371.8	59372.3	−18.31	0.22	1.34
ZTF21abkajar/SN 2021svy	13:09:21.83	+30:55:20.5	0.017	59402.7	59403.2	−17.01	0.03	0.00
ZTF21ablvzhp/SN 2021tiq	22:36:54.72	−12:33:41.9	0.024	59409.4	59411.4	−18.12	0.17	0.00
ZTF21abnlhxs/SN 2021tyw	23:05:56.45	+14:21:27.8	0.013	59417.9	59419.4	−17.85	0.63	0.00
ZTF21abnudtb/SN 2021txr	22:30:50.30	+36:33:48.2	0.026	59416.9	59418.4	−18.10	0.34	0.00
ZTF21abouuat/SN 2021ucg	22:47:37.67	+39:52:59.4	0.017	59420.4	59422.4	−17.56	0.31	0.00
ZTF21abrluay/SN 2021vfh	01:31:38.36	+31:59:23.7	0.025	59432.4	59434.4	−17.01	0.12	0.00
ZTF21abtephz/SN 2021wun	15:46:31.98	+25:25:44.6	0.023	59425.7	59427.2	−16.86	0.13	0.14
ZTF21abvcxel/SN 2021wvw	03:14:47.39	+40:15:47.7	0.010	59449.4	59449.4	−16.36	0.78	0.00
ZTF21abvcxid/SN 2021xat	02:53:03.00	+42:51:07.0	0.032	59449.0	59451.5	−17.11	0.25	0.00
ZTF21acafqtj/SN 2021yok	07:28:55.48	+20:35:09.9	0.015	59466.5	59469.5	−17.11	0.14	0.00
ZTF21accdiqz/SN 2021ywg	02:58:44.41	+17:15:48.0	0.020	59469.4	59471.4	−17.49	1.08	1.56
ZTF21acceboj/SN 2021yyg	05:16:21.03	−13:28:39.9	0.012	59471.0	59471.5	−16.51	0.40	0.00
ZTF21accwcrh/SN 2021zco	03:39:13.31	+15:59:04.9	0.032	59472.9	59474.4	−17.50	0.66	0.00
ZTF21acdcxaf/SN 2021zex	02:14:05.67	+05:10:35.5	0.031	59475.4	59476.4	−17.09	0.12	0.00
ZTF21acdezwk/SN 2021zet	21:52:13.34	−23:22:37.0	0.032	59475.2	59477.2	−18.24	0.10	0.00
ZTF21acdoyqt/SN 2021zgm	18:35:48.34	+22:27:45.2	0.013	59479.2	59480.1	−15.51	0.44	0.00
ZTF21acelnth/SN 2021zzi	01:34:39.15	+55:25:12.4	0.025	59484.9	59485.3	−17.31	0.87	0.00
ZTF21acfajbc/SN 2021aalq	09:50:40.54	+47:57:52.4	0.025	59487.0	59488.5	−18.21	0.02	0.00
ZTF21acgpjbx/SN 2021aaqn	02:37:58.18	−01:49:53.2	0.028	59492.8	59494.3	−17.39	0.11	0.00
ZTF21acgqhru/SN 2021aatd	00:59:04.17	−00:12:12.0	0.015	59492.8	59494.3	−16.63	0.07	0.00
ZTF21acgrrnl/SN 2021aayf	06:22:08.33	+50:25:44.7	0.018	59492.9	59496.4	−16.31	0.39	0.00
ZTF21acgunkr/SN 2021aaxs	08:33:35.18	+19:44:30.1	0.026	59490.5	59496.5	−17.77	0.09	0.00
ZTF21achkqhi/SN 2021abpd	02:28:52.37	−05:29:14.2	0.031	59499.9	59501.4	−17.60	0.07	0.00
ZTF21achpqlr/SN 2021abkm	18:22:37.63	+15:42:17.7	0.018	59496.7	59502.2	−16.84	0.54	0.00
ZTF21aciiaio/SN 2021abqs	11:21:37.61	+20:09:02.1	0.013	59503.0	59504.5	−16.37	0.07	0.35
ZTF21acissla/SN 2021achr	00:22:23.67	−19:47:37.0	0.025	59497.3	59503.3	−17.49	0.05	1.27
ZTF21acjglei/SN 2021acma	02:30:33.57	+30:52:17.3	0.018	59514.8	59517.3	−16.61	0.25	0.07
ZTF21ackrkqq/SN 2021addc	03:53:38.46	+37:15:47.3	0.019	59519.3	59521.3	−16.38	1.50	0.00
ZTF21aclmgzk/SN 2021adxd	00:39:22.90	+02:48:14.5	0.018	59522.3	59524.2	−16.92	0.05	1.06
ZTF21acpqqgu/SN 2021aewn	10:04:06.68	+31:11:02.7	0.021	59534.5	59536.5	−16.63	0.07	0.21
ZTF21acqxomi/SN 2021afud	09:06:41.11	−10:00:29.0	0.025	59545.4	59550.4	−16.69	0.22	0.00
ZTF22aaacxkp/SN 2022abq	13:22:56.82	+28:19:08.9	0.008	59599.2	59600.4	−16.55	0.05	0.00
ZTF22aaahubo/SN 2022cru	08:23:26.30	−04:55:06.5	0.023	59575.4	59600.3	−15.89	0.12	0.00

Table D1
(Continued)

Name	R.A. (hh:mm:ss)	Decl. (dd:mm:ss)	Redshift	$t_{\rm expl}$ (MJD)	1st Detection (MJD)	Peak mag$_r$ (mag)	$A_{V,\rm MW}$ (mag)	$A_{V,\rm host}$ (mag)
ZTF22aaaowlo/SN 2022ces	13:54:14.54	−01:26:34.6	0.024	59614.7	59623.5	−16.80	0.13	0.00
ZTF22aaevwec/SN 2022gwg	13:50:25.69	+68:33:18.1	0.031	59675.4	59676.4	−17.67	0.05	0.28
ZTF22aafsqud/SN 2022hql	13:48:06.22	+12:04:29.8	0.023	59682.8	59683.2	−17.00	0.09	0.00
ZTF22aagvgwl/SN 2022hss	12:25:38.39	+07:11:33.0	0.025	59684.8	59687.4	−17.97	0.07	0.00
ZTF22aahhgjh/SN 2022ihb	13:46:13.40	+23:05:10.9	0.030	59691.8	59693.2	−17.59	0.04	0.00
ZTF22aahyqkz/SN 2022iob	19:10:37.07	+37:39:18.7	0.028	59684.5	59689.4	−17.62	0.48	0.92
ZTF22aaijrci/SN 2022iyl	20:58:08.06	+00:27:10.0	0.030	59694.5	59698.4	−17.04	0.21	0.14
ZTF22aajipum/SN 2022joe	14:29:20.63	−22:56:09.7	0.026	59704.3	59707.3	−16.54	0.27	0.14
ZTF22aajutqu/SN 2022jux	08:07:22.25	+40:23:34.8	0.026	59711.2	59712.2	−17.56	0.16	0.00
ZTF22aajuufc/SN 2022juw	08:30:31.46	+18:12:13.7	0.027	59711.7	59712.2	−16.98	0.10	0.00
ZTF22aakdbia/SN 2022jzc	12:05:28.66	+50:31:36.8	0.002	59714.3	59715.2	−14.91	0.05	0.57
ZTF22aakdqqg/SN 2022kad	14:58:43.33	+11:37:50.8	0.020	59713.4	59714.4	−17.82	0.10	0.00
ZTF22aanrqje/SN 2022mji	09:42:54.06	+31:51:03.6	0.004	59732.7	59741.2	−15.00	0.05	0.85
ZTF22aaolwsd/SN 2022mxv	23:51:05.12	+20:09:08.9	0.014	59747.4	59751.4	−18.10	0.20	0.00
ZTF22aapargp/SN 2022niw	15:57:16.80	+19:28:28.1	0.033	59752.3	59753.3	−17.25	0.10	0.00
ZTF22aarskhm/SN 2022ohx	20:46:37.43	−2:21:50.56	0.029	59760.9	59762.4	−17.07	0.18	0.28
ZTF22aarycqo/SN 2022ojo	01:44:35.61	+37:41:50.7	0.019	59761.4	59765.4	−19.18	0.15	1.13
ZTF22aaslyzf/SN 2022oor	15:04:29.79	+02:20:18.7	0.032	59767.2	59768.2	−17.05	0.14	0.00
ZTF22aasojye/SN 2022omr	23:41:41.10	+50:02:58.9	0.023	59766.9	59768.4	−16.89	0.62	0.00
ZTF22aativsd/SN 2022ovb	22:22:29.55	+36:00:17.9	0.018	59773.4	59774.4	−18.15	0.37	0.00
ZTF22aatpwfw/SN 2022paf	22:05:26.42	−00:31:58.7	0.031	59774.4	59775.4	−16.93	0.28	0.00
ZTF22aattfmb/SN 2022oyp	18:05:13.16	+46:52:49.5	0.023	59775.8	59776.3	−16.87	0.11	0.28
ZTF22aaudjgc/SN 2022pfx	21:50:50.87	−00:50:48.9	0.027	59775.9	59778.4	−18.03	0.28	0.07
ZTF22aavbfhz/SN 2022phi	1:20:15.03	+17:49:56.49	0.029	59779.4	59782.4	−16.60	0.21	0.00
ZTF22aavobvq/SN 2022prv	15:40:07.76	+20:40:31.7	0.015	59781.7	59784.3	−18.26	0.17	0.00
ZTF22aaxzzoc/SN 2022qhc	17:16:35.13	+07:19:44.4	0.022	59789.3	59791.2	−17.28	0.48	0.42
ZTF22aaywnyg/SN 2022pru	11:59:07.65	+52:41:58.5	0.004	59787.7	59797.2	−15.42	0.07	0.00
ZTF22aazmrpx/SN 2022raj	02:03:17.52	+29:14:04.9	0.012	59798.4	59800.4	−15.20	0.15	0.00
ZTF22abadzpo/SN 2022rfz	17:22:20.39	+02:00:58.0	0.030	59799.8	59802.2	−18.65	0.49	0.00
ZTF22abbecow/SN 2022rqg	16:56:14.62	+55:01:10.3	0.029	59801.7	59805.2	−16.20	0.07	0.00
ZTF22abfavpu/SN 2022tmb	03:20:33.60	+37:29:54.8	0.019	59825.0	59825.5	−17.10	1.04	0.00
ZTF22abfwxtr/SN 2022udq	00:05:55.84	+22:29:26.3	0.022	59834.7	59839.2	−16.96	0.20	0.00
ZTF22abfxkdm/SN 2022ubb	23:08:58.34	+12:02:39.0	0.016	59834.3	59839.3	−16.57	0.24	0.00
ZTF22abgwgsv/SN 2022vpm	17:22:32.88	+26:46:04.2	0.022	59842.7	59843.2	−17.80	0.12	0.00
ZTF22abhsxph/SN 2022vyc	04:33:10.32	+76:34:05.3	0.026	59844.9	59846.4	−17.01	0.43	0.00
ZTF22abitour/SN 2022wbr	04:29:15.65	+40:14:46.9	0.020	59838.0	59847.5	−16.34	1.67	0.00
ZTF22abkbjsb/SN 2022vym	08:54:01.09	+18:41:18.1	0.015	59849.0	59853.5	−16.48	0.06	0.21
ZTF22abkhrkd/SN 2022wol	01:51:27.78	+36:03:51.5	0.018	59853.9	59854.3	−16.02	0.21	0.00
ZTF22ablnrcv/SN 2022xav	09:39:17.64	+32:18:38.3	0.023	59857.0	59858.5	−16.96	0.05	0.42
ZTF22abmsaxp/SN 2022xjk	02:16:32.50	−11:20:59.4	0.013	59860.9	59861.4	−17.15	0.10	0.00
ZTF22abnujbv/SN 2022xus	06:54:05.13	+08:34:13.3	0.009	59869.4	59871.4	−16.42	0.60	0.00
ZTF22abpxxil/SN 2022yma	03:08:48.32	−07:02:06.5	0.029	59871.9	59873.3	−17.16	0.20	0.49
ZTF22abrexqa/SN 2022yyz	19:07:01.55	+28:59:50.0	0.013	59880.1	59881.1	−17.52	0.64	0.00
ZTF22absqhkw/SN 2022zkc	04:47:58.59	−16:39:37.0	0.032	59885.4	59887.4	−17.40	0.14	0.00
ZTF22abssiet/SN 2022zmb	10:38:43.18	+56:33:14.4	0.014	59885.5	59887.5	−15.72	0.02	0.07
ZTF22abtcsyd/SN 2022zxt	08:40:16.38	+56:02:36.0	0.026	59891.5	59893.4	−17.25	0.10	0.00
ZTF22abtspsw/SN 2022aagp	09:10:41.90	+07:12:20.3	0.005	59895.4	59897.4	−17.09	0.12	0.00
ZTF22abulusd/SN 2022aatx	09:15:15.32	+11:53:04.6	0.017	59899.4	59902.5	−17.27	0.08	0.49
ZTF22abvaetz/SN 2022aang	07:59:21.83	+18:06:40.9	0.016	59894.5	59901.5	−15.44	0.08	0.00
ZTF22abxomzd/SN 2022acbu	02:30:43.15	−02:55:56.9	0.019	59906.8	59910.2	−18.75	0.08	3.11
ZTF22abyivoq/SN 2022acko	03:19:38.98	−19:23:42.8	0.006	59917.8	59922.2	−15.83	0.08	0.00
ZTF22abyivxh/SN 2022acwe	02:28:07.20	−05:43:37.0	0.030	59917.8	59922.2	−17.22	0.07	0.00
ZTF22abyohff/SN 2022acrl	11:34:21.03	+15:39:49.2	0.017	59913.5	59923.5	−16.32	0.12	0.00
ZTF22abyokkf/SN 2022acri	14:34:19.17	+25:52:55.4	0.022	59915.0	59923.5	−17.22	0.08	0.00
ZTF22abzdzek/SN 2022adtt	01:14:05.28	+38:07:05.2	0.027	59930.2	59932.1	−16.80	0.13	0.00

Table D1
(Continued)

Name	R.A. (hh:mm:ss)	Decl. (dd:mm:ss)	Redshift	$t_{\rm expl}$ (MJD)	1st Detection (MJD)	Peak mag$_r$ (mag)	$A_{V,\rm MW}$ (mag)	$A_{V,\rm host}$ (mag)
ZTF22abzqwmp/SN 2022adth	10:15:39.94	+45:56:25.2	0.031	59932.8	59933.3	−16.84	0.02	0.00
ZTF22acahbko/SN 2022advr	10:22:48.99	+03:45:18.7	0.033	59934.5	59935.4	−16.61	0.10	0.00
ZTF23aaaatjn/SN 2023cf	04:26:49.49	+29:56:59.8	0.018	59945.8	59951.2	−18.51	1.26	0.00
ZTF23aaaigqy/SN 2023fu	03:06:21.26	+36:01:11.1	0.016	59948.7	59957.1	−17.97	0.66	0.00
ZTF23aaarmtb/SN 2023qh	09:07:15.44	+37:12:54.8	0.024	59947.4	59957.4	−15.89	0.06	0.00
ZTF23aaavxye/SN 2023abq	15:34:33.34	+41:08:11.6	0.032	59962.7	59967.5	−17.63	0.07	0.00
ZTF23aaazdla/SN 2023wn	13:36:04.57	−01:35:39.7	0.015	59962.5	59968.5	−16.79	0.09	0.00
ZTF23aabngtm/SN 2023axu	06:45:55.32	−18:13:53.5	0.003	59970.3	59972.3	−17.27	1.06	0.00
ZTF23aabtmzm/SN 2023blw	07:28:09.44	+52:28:17.5	0.022	59975.7	59979.2	−18.35	0.16	2.97
ZTF23aacdlsh/SN 2023bmd	15:10:08.83	+46:06:23.2	0.020	59982.5	59984.5	−16.69	0.07	0.00
ZTF23aacjetk/SN 2023buy	08:20:53.69	+39:14:29.7	0.029	59988.3	59991.2	−17.87	0.12	0.00
ZTF23aackdba/SN 2023bql	08:11:27.82	+08:56:24.7	0.019	59984.8	59985.3	−16.51	0.07	0.28
ZTF23aackjhs/SN 1995al	09:50:56.03	+33:33:11.0	0.005	59989.8	59992.3	−14.88	0.04	0.07
ZTF23aaflnok/SN 2023fub	07:40:26.79	+25:08:00.2	0.029	60047.2	60049.2	−17.22	0.12	0.00
ZTF23aafumlg/SN 2023fou	12:40:20.46	−10:02:55.1	0.026	60047.8	60050.3	−17.85	0.10	0.00
ZTF23aagkajy/SN 2023gdt	10:30:10.64	+43:21:23.4	0.014	60050.2	60051.2	−15.42	0.03	0.71
ZTF23aagkutf/SN 2023ghl	11:09:11.73	+53:21:43.9	0.027	60052.2	60053.2	−17.24	0.03	0.00
ZTF23aagqyym/SN 2023gjg	09:07:17.96	+37:30:12.6	0.030	60054.2	60055.2	−17.08	0.05	0.00
ZTF23aahqvtz/SN 2023gss	14:04:23.54	−27:08:58.1	0.021	60058.8	60059.3	−17.07	0.19	0.00
ZTF23aaiecnn/SN 2023gxq	10:18:12.24	+34:40:19.7	0.029	60061.2	60062.2	−16.51	0.04	0.00
ZTF23aailjjs/SN 2023hcp	16:48:42.72	+35:56:57.4	0.031	60062.4	60063.4	−17.91	0.05	0.00
ZTF23aaitpjv/SN 2023hlf	12:26:26.17	+31:13:32.2	0.002	60053.3	60054.4	−16.53	0.05	5.09
ZTF23aajrmfh/SN 2023ijd	12:36:32.47	+11:13:19.7	0.007	60078.2	60079.0	−15.39	0.09	0.00
ZTF23aajsjon/SN 2023hzt	13:30:01.55	+75:34:09.0	0.030	60071.9	60076.4	−17.05	0.10	0.00
ZTF23aakirso/SN 2023jid	22:40:43.23	+36:38:39.5	0.027	59994.8	60054.5	−16.12	0.42	0.00
ZTF23aamfqxc/SN 2023jri	23:30:27.09	+30:13:11.2	0.015	60094.2	60097.4	−18.81	0.40	0.28
ZTF23aamqycj/SN 2023jvi	13:31:22.27	+25:37:01.0	0.025	60094.8	60097.3	−17.03	0.03	0.00
ZTF23aamzlzc/SN 2023kne	17:25:19.11	+58:49:02.6	0.028	60095.4	60097.3	−15.81	0.10	0.00
ZTF23aanymcl/SN 2023kzz	17:17:06.29	−14:54:05.1	0.028	60106.8	60110.3	−17.24	1.26	0.00
ZTF23aanzmoz/SN 2023kyi	19:16:43.95	−17:30:35.0	0.030	60105.9	60108.4	−17.00	0.33	0.00
ZTF23aaomzth/SN 2023rpu	09:23:47.48	+42:11:12.1	0.014	60105.2	60113.2	−16.56	0.05	0.00
ZTF23aaphnyz/SN 2023lkw	16:48:36.21	+41:36:02.6	0.031	60117.8	60118.2	−18.07	0.06	0.00
ZTF23aaqknaw/SN 2023lzn	00:55:07.58	+31:32:47.6	0.018	60124.4	60128.4	−17.37	0.17	0.85
ZTF23aaqtckr/SN 2023mpj	14:34:24.79	+02:53:04.9	0.030	60120.2	60120.3	−16.62	0.10	0.00
ZTF23aaqwpio/SN 2023nca	16:39:26.36	+11:12:45.3	0.023	60129.3	60135.2	−15.61	0.14	0.00
ZTF23aasbvab/SN 2023ngy	22:18:30.18	+29:14:41.0	0.021	60139.9	60140.3	−16.80	0.22	0.00
ZTF23aasrcyv/SN 2023nlu	00:45:09.04	−09:37:38.3	0.020	60142.5	60143.4	−16.78	0.10	0.00
ZTF23aasyvbf/SN 2023nmh	00:37:38.73	−04:16:53.2	0.020	60142.4	60144.5	−15.93	0.10	0.00
ZTF23aaxadel/SN 2023pbg	00:14:54.90	+26:20:00.4	0.025	60166.9	60168.4	−16.88	0.11	0.00
ZTF23aazprcc/SN 2023vhb	12:19:13.19	+22:25:42.4	0.022	60180.1	60181.1	−17.20	0.07	0.21
ZTF23abadrow/SN 2023qxp	21:56:14.96	+02:10:27.8	0.028	60175.9	60178.4	−16.65	0.15	0.00
ZTF23abascqa/SN 2023rbk	03:15:20.60	+41:36:53.5	0.020	60186.4	60187.4	−17.96	0.38	0.00
ZTF23abaxtlq/SN 2023rix	02:47:56.84	+41:14:48.3	0.013	60191.9	60192.4	−16.37	0.23	0.00
ZTF23abbsxzs/SN 2023rtq	04:51:46.59	+38:56:10.0	0.013	60193.4	60195.4	−17.56	2.68	0.57
ZTF23abbtkrv/SN 2023rvo	08:49:16.37	+36:07:14.8	0.025	60193.0	60194.5	−17.05	0.09	0.00
ZTF23aberpzw/SN 2023swf	21:05:58.52	−14:50:30.3	0.023	60201.7	60203.2	−16.66	0.17	0.00
ZTF23abhruov/SN 2023ucx	03:59:54.88	+32:36:41.1	0.018	60210.4	60215.4	−17.08	0.65	1.91
ZTF23abhyroo/SN 2023udb	04:25:05.77	−10:18:51.9	0.033	60219.0	60221.5	−17.25	0.25	0.00
ZTF23abhzfww/SN 2023twg	08:45:54.52	+12:47:12.2	0.030	60214.5	60220.5	−17.62	0.09	0.00
ZTF23abiewbt/SN 2023ujp	15:57:33.01	+20:02:54.2	0.033	60222.1	60223.1	−17.36	0.12	0.00
ZTF23abjwgre/SN 2023vcg	23:56:05.87	+29:22:40.5	0.023	60231.3	60231.3	−16.70	0.17	0.00
ZTF23abkhajf/SN 2023vcj	07:55:15.92	+53:44:47.7	0.025	60228.5	60232.5	−17.38	0.09	0.07
ZTF23abmoxlu/SN 2023vog	09:45:09.63	+68:35:11.8	0.015	60237.4	60238.4	−17.59	0.28	0.00
ZTF23abndgbw/SN 2023way	21:24:11.15	+15:59:22.9	0.018	60240.7	60242.2	−16.68	0.31	0.00
ZTF23abnogui/SN 2023wcr	12:23:31.29	+74:57:01.3	0.005	60240.5	60244.5	−15.58	0.09	0.00

Table D1
(Continued)

Name	R.A. (hh:mm:ss)	Decl. (dd:mm:ss)	Redshift	t_{expl} (MJD)	1st Detection (MJD)	Peak mag$_r$ (mag)	$A_{V,MW}$ (mag)	$A_{V,host}$ (mag)
ZTF23abonlit/SN 2023wuj	08:26:18.36	+02:55:28.6	0.031	60247.0	60248.5	−16.79	0.14	0.00
ZTF23abphqjk/SN 2023xgn	03:02:48.82	−15:42:21.6	0.031	60253.9	60254.4	−17.42	0.15	0.00
ZTF23abqwald/SN 2023xvo	11:20:24.29	+28:17:55.4	0.033	60234.0	60234.5	−16.90	0.05	0.21
ZTF23absdcgi/SN 2023zcu	06:01:06.82	−23:40:29.3	0.006	60288.2	60289.3	−16.73	0.09	0.00
ZTF23abvommm/SN 2023acbr	02:27:03.18	−09:25:02.3	0.016	60300.7	60305.2	−15.57	0.08	0.00
ZTF24aaabbse/SN 2023achj	08:36:07.46	+25:06:47.0	0.023	60303.9	60311.3	−17.79	0.10	0.00
ZTF24aaarlvj/SN 2024V	11:52:01.50	+57:41:37.4	0.031	60300.0	60308.5	−16.49	0.04	0.00
ZTF24aaasazz/SN 2024ov	11:50:28.79	−18:34:42.8	0.023	60291.0	60291.6	−16.03	0.10	0.00
ZTF24aabppgn/SN 2024wp	11:24:39.25	+14:56:52.9	0.014	60320.5	60325.5	−15.52	0.10	0.00
ZTF24aabpzuz/SN 2024vs	07:51:07.27	+72:57:57.4	0.010	60317.9	60321.5	−16.70	0.08	0.00
ZTF24aabsmvc/SN 2024ws	08:28:46.69	+73:45:08.6	0.012	60318.9	60322.3	−16.15	0.07	0.00
ZTF24aadkwni/SN 2024aul	10:21:53.24	+00:17:44.3	0.021	60330.7	60335.4	−17.77	0.13	0.28
ZTF24aaejehf/SN 2024bzq	11:44:33.94	+36:26:41.2	0.033	60346.4	60351.4	−17.97	0.05	0.00
ZTF24aaejjps/SN 2024btx	11:54:55.45	+29:20:34.5	0.021	60346.4	60351.4	−16.04	0.06	0.00
ZTF24aaejvcx/SN 2024atk	13:18:31.13	−14:36:39.1	0.010	60343.2	60351.4	−16.54	0.22	0.00
ZTF24aaemydm/SN 2024chx	09:54:28.51	−18:38:10.8	0.013	60352.8	60354.2	−18.01	0.13	0.00
ZTF24aafqzur/SN 2024daa	14:25:57.20	−02:23:32.2	0.031	60355.4	60355.5	−16.72	0.15	0.00
ZTF24aagiwoi/SN 2024dhi	11:13:08.67	+05:04:28.3	0.027	60360.9	60363.4	−16.65	0.20	0.00
ZTF24aagupsf/SN 2024egd	16:30:41.48	+44:30:40.0	0.032	60372.0	60374.5	−17.47	0.04	0.00
ZTF24aahalmb/SN 2024ees	12:32:42.19	+14:32:27.4	0.024	60376.8	60379.4	−16.52	0.11	0.00
ZTF24aahewml/SN 2024etq	18:13:41.23	+10:56:03.8	0.022	60381.0	60387.5	−16.60	0.51	0.00
ZTF24aahgmyj/SN 2024epy	09:46:46.54	+13:31:53.4	0.024	60384.2	60388.2	−16.77	0.12	0.64
ZTF24aahmgck/SN 2024faf	11:28:57.38	+73:02:11.9	0.021	60385.8	60388.3	−16.85	0.13	1.27
ZTF24aahwfsa/SN 2024fas	10:51:55.36	+37:35:23.9	0.026	60393.4	60396.4	−15.80	0.04	0.00
ZTF24aajxppf/SN 2024grw	17:58:21.63	+09:40:53.5	0.021	60415.5	60416.5	−18.01	0.48	0.00
ZTF24aakzive/SN 2024hpg	21:31:43.20	+0:21:43.71	0.029	60427.7	60430.4	−17.53	0.14	0.00
ZTF24aalceob/SN 2024hme	16:05:57.74	+27:11:21.00	0.031	60418.9	60423.4	−16.09	0.10	0.00
ZTF24aamzqsv/SN 2024izq	9:24:57.24	+40:23:58.49	0.028	60440.2	60441.2	−16.29	0.04	0.00
ZTF24aaozxhx/SN 2024jlf	14:37:42.32	+2:17:04.17	0.006	60457.3	60458.2	−16.99	0.11	0.00
ZTF24aaplfjd/SN 2024jxm	0:58:01.36	+30:42:23.84	0.016	60460.0	60460.5	−16.00	0.18	0.00
ZTF24aarajmv/SN 2024ldu	19:54:05.17	+49:56:47.25	0.025	60466.4	60469.4	−16.26	0.50	0.00
ZTF24aarvbxj/SN 2024lby	20:22:40.78	−8:10:41.95	0.020	60472.4	60473.4	−17.56	0.17	0.00
ZTF24aasktmr/SN 2024lss	16:31:22.18	+22:42:08.73	0.024	60479.8	60480.2	−17.19	0.13	0.00
ZTF24aatifzm/SN 2024mxq	14:44:05.84	+9:16:47.52	0.031	60480.8	60484.2	−16.83	0.08	0.00

Note. The peak absolute magnitudes have been measured by assuming Milky Way extinction ($A_{V,MW}$) and host galaxy extinction ($A_{V,host}$) as described in Section 4. The t_{expl} column shows the explosion epoch. The Peak mag$_r$ shows the peak r-band absolute magnitude. A machine-readable version of the full sample table is available in DOI:10.5281/zenodo.14538857.

ORCID iDs

Kaustav K. Das https://orcid.org/0000-0001-8372-997X
Mansi M. Kasliwal https://orcid.org/0000-0002-5619-4938
Christoffer Fremling https://orcid.org/0000-0002-4223-103X
Jesper Sollerman https://orcid.org/0000-0003-1546-6615
Daniel A. Perley https://orcid.org/0000-0001-8472-1996
Kishalay De https://orcid.org/0000-0002-8989-0542
Anastasios Tzanidakis https://orcid.org/0000-0003-0484-3331
Scott Adams https://orcid.org/0000-0001-5855-5939
Shreya Anand https://orcid.org/0000-0003-3768-7515
Rachel J. Bruch https://orcid.org/0000-0002-0786-7307
Ping Chen https://orcid.org/0000-0003-0853-6427
David O. Cook https://orcid.org/0000-0002-6877-7655
Sofia Covarrubias https://orcid.org/0000-0003-1858-561X
Nicholas Earley https://orcid.org/0000-0001-6627-9903
Anna Y. Q. Ho https://orcid.org/0000-0002-9017-3567
Viraj Karambelkar https://orcid.org/0000-0003-2758-159X
S. R. Kulkarni https://orcid.org/0000-0001-5390-8563
Theophile Jegou du Laz https://orcid.org/0009-0003-6181-4526
Chang Liu https://orcid.org/0000-0002-7866-4531
Adam A. Miller https://orcid.org/0000-0001-9515-478X
Guy Nir https://orcid.org/0000-0002-7501-5579
Priscila J. Pessi https://orcid.org/0000-0002-8041-8559
Nabeel Rehemtulla https://orcid.org/0000-0002-5683-2389
Sam Rose https://orcid.org/0000-0003-4725-4481

Ben Rusholme https://orcid.org/0000-0001-7648-4142
Steve Schulze https://orcid.org/0000-0001-6797-1889
Yashvi Sharma https://orcid.org/0000-0003-4531-1745
Avinash Singh https://orcid.org/0000-0003-2091-622X
Roger Smith https://orcid.org/0000-0001-7062-9726
Yu-Jing Qin https://orcid.org/0000-0003-3658-6026
Jacob Wise https://orcid.org/0000-0003-0733-2916
Avery Wold https://orcid.org/0000-0002-9998-6732
Lin Yan https://orcid.org/0000-0003-1710-9339
Yuhan Yao https://orcid.org/0000-0001-6747-8509
Erez Zimmerman https://orcid.org/0000-0001-8985-2493

References

Adams, S. M., Kochanek, C. S., Prieto, J. L., et al. 2016, MNRAS, 460, 1645
Ambikasaran, S., Foreman-Mackey, D., Greengard, L., Hogg, D. W., & O'Neil, M. 2015, ITPAM, 38, 252
Arcavi, I., Gal-Yam, A., Cenko, S. B., et al. 2012, ApJL, 756, L30
Barker, B. L., Harris, C. E., Warren, M. L., O'Connor, E. P., & Couch, S. M. 2022, ApJ, 934, 67
Barnsley, R. M., Smith, R. J., & Steele, I. A. 2012, AN, 333, 101
Bellm, E. C., Kulkarni, S. R., Graham, M. J., et al. 2019, PASP, 131, 018002
Bellm, E. C., & Sesar, B. 2016, pyraf-dbsp: Reduction Pipeline for the Palomar Double Beam Spectrograph, Astrophysics Source Code Library, ascl:1602.002
Blagorodnova, N., Neill, J. D., Walters, R., et al. 2018, PASP, 130, 035003
Blondin, S., & Tonry, J. L. 2007, in AIP Conf. Ser. 924, The Multicolored Landscape of Compact Objects and Their Explosive Origins, ed. T. di Salvo et al. (Melville, NY: AIP), 312
Bostroem, K. A., Dessart, L., Hillier, D. J., et al. 2023, ApJL, 953, L18
Botticella, M. T., Pastorello, A., Smartt, S. J., et al. 2009, MNRAS, 398, 1041
Botticella, M. T., Smartt, S. J., Kennicutt, R. C., et al. 2012, A&A, 537, A132
Burrows, A., Radice, D., & Vartanyan, D. 2019, MNRAS, 485, 3153
Burrows, A., & Vartanyan, D. 2021, Natur, 589, 29
Burrows, A., Wang, T., & Vartanyan, D. 2024, ApJL, 964, 16
Cai, Y. Z., Pastorello, A., Fraser, M., et al. 2021, A&A, 654, A157
Cappellaro, E., Botticella, M. T., Pignata, G., et al. 2015, A&A, 584, A62
Cardelli, J. A., Clayton, G. C., & Mathis, J. S. 1989, ApJ, 345, 245
Cook, D. O., Kasliwal, M. M., Van Sistine, A., et al. 2019, ApJ, 880, 7
Coughlin, M. W., Bloom, J. S., Nir, G., et al. 2023, ApJS, 267, 31
Crockett, R. M., Smartt, S. J., Pastorello, A., et al. 2011, MNRAS, 410, 2767
D'Andrea, C. B., Sako, M., Dilday, B., et al. 2010, ApJ, 708, 661
Das, K. K., Fremling, C., Kasliwal, M. M., et al. 2024a, ApJL, 969, L11
Das, K. K., Kasliwal, M. M., Fremling, C., et al. 2023, ApJ, 959, 12
Das, K. K., Kasliwal, M. M., Laz, T. J. D., et al. 2025, TNSAN, 64, 1
Das, K. K., Kasliwal, M. M., Sollerman, J., et al. 2024b, ApJ, 972, 91
Dastidar, R., Misra, K., Valenti, S., et al. 2025, A&A, 694, 18
De, K., Kasliwal, M. M., Tzanidakis, A., et al. 2020, ApJ, 905, 58
de Jaeger, T., Anderson, J. P., Galbany, L., et al. 2018, MNRAS, 476, 4592
Dekany, R., Smith, R. M., Riddle, R., et al. 2020, PASP, 132, 038001
Djupvik, A. A., & Andersen, J. 2010, Highlights of Spanish Astrophysics V. Astrophysics and Space Science Proceedings (Berlin, Heidelberg: Springer), 211
Eldridge, J. J., Guo, N. Y., Rodrigues, N., Stanway, E. R., & Xiao, L. 2019, PASA, 36, e041
Elias-Rosa, N., Van Dyk, S. D., Li, W., et al. 2011, ApJ, 742, 6
Foreman-Mackey, D., Hogg, D. W., Lang, D., & Goodman, J. 2013, PASP, 125, 306
Fox, O. D., Khandrika, H., Rubin, D., et al. 2021, MNRAS, 506, 4199
Fraser, M., Ergon, M., Eldridge, J. J., et al. 2011, MNRAS, 417, 1417
Fraser, M., Maund, J. R., Smartt, S. J., et al. 2014, MNRAS, 439, L56
Fraser, M., Takáts, K., Pastorello, A., et al. 2010, ApJL, 714, L280
Fremling, C., Miller, A. A., Sharma, Y., et al. 2020, ApJ, 895, 32
Graham, M. J., Kulkarni, S. R., Bellm, E. C., et al. 2019, PASP, 131, 078001
Helou, G., Madore, B. F., Schmitz, M., et al. 1991, in Databases and On-line Data in Astronomy, ed. M. A. Albrecht & D. Egret (Dordrecht: Springer), 89
Ho, A. Y. Q., Perley, D. A., Gal-Yam, A., et al. 2023, ApJ, 949, 120
Hopkins, A. M., & Beacom, J. F. 2006, ApJ, 651, 142
Horiuchi, S., Beacom, J. F., Bothwell, M. S., & Thompson, T. A. 2013, ApJ, 769, 113
Horiuchi, S., Beacom, J. F., Kochanek, C. S., et al. 2011, ApJ, 738, 154
Howell, D. A., Sullivan, M., Perrett, K., et al. 2005, ApJ, 634, 1190
Ivezić, Ž., Tyson, J. A., Acosta, E., et al. 2008, arXiv:0805.2366
Jacobson-Galán, W. V., Venkatraman, P., Margutti, R., et al. 2022, ApJ, 932, 58
Jäger Zoltán, J., Vinkó, J., Bíró, B. I., et al. 2020, MNRAS, 496, 3725
Janka, H.-T. 2012, ARNPS, 62, 407
Jencson, J. E., Adams, S. M., Bond, H. E., et al. 2019a, ApJL, 880, L20
Jencson, J. E., Kasliwal, M. M., Adams, S. M., et al. 2019b, ApJ, 886, 40
Jerkstrand, A., Ertl, T., Janka, H. T., et al. 2018, MNRAS, 475, 277
Karambelkar, V. R., Kasliwal, M. M., Blagorodnova, N., et al. 2023, ApJ, 948, 137
Kasliwal, M. M., Cannella, C., Bagdasaryan, A., et al. 2019, PASP, 131, 038003
Kim, Y. L., Rigault, M., Neill, J. D., et al. 2022, PASP, 134, 024505
Kochanek, C. S., Khan, R., & Dai, X. 2012, ApJ, 759, 20
Kondo, I., Sumi, T., Koshimoto, N., et al. 2023, AJ, 165, 254
Kozyreva, A., Baklanov, P., Jones, S., Stockinger, G., & Janka, H.-T. 2021, MNRAS, 503, 797
Kozyreva, A., Janka, H.-T., Kresse, D., Taubenberger, S., & Baklanov, P. 2022, MNRAS, 514, 4173
Leung, S.-C., & Fuller, J. 2020, ApJ, 900, 99
Li, W., Leaman, J., Chornock, R., et al. 2011, MNRAS, 412, 1441
Li, W., Van Dyk, S. D., Filippenko, A. V., et al. 2006, ApJ, 641, 1060
Lisakov, S. M., Dessart, L., Hillier, D. J., Waldman, R., & Livne, E. 2017, MNRAS, 466, 34
Lourie, N. P., Baker, J. W., Burruss, R. S., et al. 2020, Proc. SPIE, 11447, 114479K
Masci, F. J., Laher, R. R., Rusholme, B., et al. 2019, PASP, 131, 018003
Masci, F. J., Laher, R. R., Rusholme, B., et al. 2023, arXiv:2305.16279
Mattila, S., Dahlen, T., Efstathiou, A., et al. 2012, ApJ, 756, 111
Mattila, S., Smartt, S. J., Eldridge, J. J., et al. 2008, ApJL, 688, L91
Maund, J. R., Fraser, M., Smartt, S. J., et al. 2013, MNRAS, 431, L102
Maund, J. R., Reilly, E., & Mattila, S. 2014, MNRAS, 438, 938
Maund, J. R., & Smartt, S. J. 2009, Sci, 324, 486
Maund, J. R., Smartt, S. J., & Danziger, I. J. 2005, MNRAS, 364, L33
Miyaji, S., Nomoto, K., Yokoi, K., & Sugimoto, D. 1980, PASJ, 32, 303
Moore, T., Gillanders, J. H., Nicholl, M., et al. 2025, ApJL, 980, 13
Moriya, T. J., Mazzali, P. A., Tominaga, N., et al. 2017, MNRAS, 466, 2085
Müller, B. 2016, PASA, 33, e048
Müller-Bravo, T. E., Gutiérrez, C. P., Sullivan, M., et al. 2020, MNRAS, 497, 361
Nomoto, K. 1984, ApJ, 277, 791
Oke, J. B., Cohen, J. G., Carr, M., et al. 1995, PASP, 107, 375
Oke, J. B., & Gunn, J. E. 1982, PASP, 94, 586
O'Neill, D., Kotak, R., Fraser, M., et al. 2019, A&A, 622, L1
Perley, D. A. 2019, PASP, 131, 084503
Perley, D. A., Sollerman, J., Schulze, S., et al. 2022, ApJ, 927, 180
Piascik, A. S., Steele, I. A., Bates, S. D., et al. 2014, Proc. SPIE, 9147, 91478H
Poznanski, D., Prochaska, J. X., & Bloom, J. S. 2012, MNRAS, 426, 1465
Prochaska, J., Hennawi, J., Westfall, K., et al. 2020, JOSS, 5, 2308
Pumo, M. L., Zampieri, L., Spiro, S., et al. 2017, MNRAS, 464, 3013
Reguitti, A., Pumo, M. L., Mazzali, P. A., et al. 2021, MNRAS, 501, 1059
Rigault, M., Neill, J. D., Blagorodnova, N., et al. 2019, A&A, 627, A115
Roberson, M., Fremling, C., & Kasliwal, M. 2022, JOSS, 7, 3612
Rodríguez, Ó. 2022, MNRAS, 515, 897
Rodríguez, Ó., Meza, N., Pineda-García, J., & Ramirez, M. 2021, MNRAS, 505, 1742
Rose, S., Lau, R. M., Jencson, J. E., et al. 2025, ApJL, 980, 11
Salpeter, E. E. 1955, ApJ, 121, 161
Sana, H., de Mink, S. E., de Koter, A., et al. 2012, Sci, 337, 444
Sanders, N. E., Soderberg, A. M., Gezari, S., et al. 2015, ApJ, 799, 208

Sandoval, M. A., Hix, W. R., Messer, O. E. B., Lentz, E. J., & Harris, J. A. 2021, ApJ, 921, 113
Sawada, R., Kashiyama, K., & Suwa, Y. 2022, ApJ, 927, 223
Schlafly, E. F., & Finkbeiner, D. P. 2011, ApJ, 737, 103
Shrestha, M., Pearson, J., Wyatt, S., et al. 2024, ApJ, 961, 247
Smartt, S. J. 2015, PASA, 32, e016
Soon, J., Adams, D., De, K., et al. 2020, Proc. SPIE, 11203, 1120307
Spiro, S., Pastorello, A., Pumo, M. L., et al. 2014, MNRAS, 439, 2873
Stockinger, G., Janka, H. T., Kresse, D., et al. 2020, MNRAS, 496, 2039
Stritzinger, M. D., Taddia, F., Burns, C. R., et al. 2018, A&A, 609, A135
Sukhbold, T., Ertl, T., Woosley, S. E., Brown, J. M., & Janka, H. T. 2016, ApJ, 821, 38
Taylor, M., Cinabro, D., Dilday, B., et al. 2014, ApJ, 792, 135
Teja, R. S., Goldberg, J. A., Sahu, D. K., et al. 2024, ApJ, 974, 44
Thompson, T. A., Prieto, J. L., Stanek, K. Z., et al. 2009, ApJ, 705, 1364
Tomasella, L., Cappellaro, E., Fraser, M., et al. 2013, MNRAS, 434, 1636
Turatto, M., Mazzali, P. A., Young, T. R., et al. 1998, ApJL, 498, L129
Valerin, G., Pastorello, A., Reguitti, A., et al. 2025, A&A, 695, A42
Valerin, G., Pumo, M. L., Pastorello, A., et al. 2022, MNRAS, 513, 4983
van der Walt, S., Crellin-Quick, A., & Bloom, J. 2019, JOSS, 4, 1247
Van Dyk, S. D., Bostroem, K. A., Zheng, W., et al. 2023, MNRAS, 524, 2186
Woosley, S. E., & Heger, A. 2015, ApJ, 810, 34
Xiao, L., & Eldridge, J. J. 2015, MNRAS, 452, 2597
Yang, S., Sollerman, J., Strotjohann, N. L., et al. 2021, A&A, 655, A90
Zapartas, E., de Mink, S. E., Justham, S., et al. 2021, A&A, 645, A6
Zapartas, E., de Mink, S. E., Justham, S., et al. 2019, A&A, 631, A5